

Surfaceome dynamics during neuronal development and synaptic plasticity reveal system-wide surfaceome reorganization independent of global proteostasis

Marc van Oostrum^{1,2,3,5}, Benjamin Campbell^{1,4}, Maik Müller^{2,3,5}, Patrick G. A. Pedrioli^{2,5}, Shiva K. Tyagarajan^{1,4}, Bernd Wollscheid^{1,2,3,5}

¹Neuroscience Center Zurich, Zurich, Switzerland

²Institute of Molecular Systems Biology at the Department of Biology, ETH Zurich, Zurich 8093, Switzerland

³Biomedical Proteomics Platform, Department of Health Sciences and Technology, ETH Zurich, 8093 Zurich, Switzerland

⁴Institute of Pharmacology and Toxicology, University of Zurich, Zurich, Switzerland.

⁵Swiss Institute of Bioinformatics (SIB), Switzerland

Neurons are highly compartmentalized cells with tightly controlled subcellular protein organization. While broad brain transcriptome, connectome and global proteome maps are being generated, system-wide analysis of temporal protein dynamics at the subcellular level are currently lacking for neuronal development and synapse formation. We performed a temporally-resolved surfaceome analysis of developing primary neuron cultures to a depth of 1000 *bona fide* surface proteins and reveal dynamic surface protein clusters that reflect the functional requirements during distinct stages of neuronal development. Moreover, our data shows that synaptic proteins are globally trafficked to the surface prior to synapse formation. Direct comparison of surface and total protein pools demonstrates that, depending on the time scale, surface abundance changes can correlate or differ from total protein abundance. The uncoupling of surface and total abundance changes has direct functional implications as shown in the context of synaptic vesicle transport. To demonstrate the utility of our approach we analyzed the surfaceome modulation in response to homeostatic synaptic scaling and found dynamic remodeling of the neuronal surface, which was largely independent of global proteostasis, indicative of wide-spread regulation on the level of surface trafficking. Finally, we present a quantitative analysis of the neuronal surface during early-phase long-term potentiation (LTP) and reveal fast externalization of diverse classes of surface proteins beyond the AMPA receptor, providing new insights into the requirement of exocytosis for LTP. Our resource and finding of organizational principles highlight the importance of subcellular resolution for systems-level understanding of cellular processes, which are typically masked by broad omics-style approaches.

Introduction

Assembly of neurons into higher order circuits via synaptic connectivity enables the mammalian brain to perform incredibly complex cognition. The quality, quantity, and interactions of cell-surface proteins drive neuronal development and activity-dependent synaptic plasticity¹⁻⁵. Emerging evidence suggests that the diversity of extracellular proteins is crucial for synapse formation and wiring specificity⁶. Although the molecular mechanisms remain elusive, it has been hypothesized that different surface molecules act in a combinatorial fashion without obvious hierarchy in signaling⁷. In order to understand, manipulate, and model the underlying molecular principles, the key cell-surface players involved in neuronal development and plasticity need to be identified and the dynamic interplay of these factors have to be characterized⁸.

Comprehensive analysis of the neuronal surface-exposed proteome, referred to as the surfaceome, remains challenging mainly for technical reasons. Global protein analyses have provided in-depth inventories of protein expression across mouse brain regions and cell types^{9,10}, characterized proteome dynamics during neuronal differentiation¹¹, and identified newly synthesized proteins during homeostatic scaling^{12,13}. However, such analyses describe the total cellular protein pool and disregard subcellular spatial organization. Proteomics analysis using mass spectroscopy (MS) in combination with chemical labeling or fractionation schemes have been used to study the composition of synaptic vesicles¹⁴, the postsynaptic compartment¹⁵⁻¹⁷, the presynaptic active zone¹⁸, synaptosomes¹⁹, the synaptic cleft²⁰, the axonal proteome²¹, interactomes of neuronal receptors²²⁻²⁵, and the neuronal spatial proteome²⁶. Similarly, the plasma membrane proteome of primary neuronal cultures has been investigated using metabolic labeling and subsequent enrichment of glycoproteins^{27,28}. This approach enables quantitative comparison of the plasma membrane glycoproteome between different conditions but cannot unambiguously define the acute surfaceome. The protein-level affinity enrichment employed precludes *a priori* separation of enriched surface proteins from nonspecific background, thus there must be prior knowledge of surface localization to filter *post-hoc* for known plasma membrane proteins. Furthermore, chemical labeling or fractionation strategies are labor intensive, especially for multiplexed applications with primary neuronal cultures or tissue. To quantitatively link spatial proteotypes to functional phenotypes and to provide a systems-level perspective on spatial dynamics for a more complete understanding of the underlying cellular biology it is necessary to capture the dynamics of protein expression at the subcellular level²⁹.

Recently, we reported a miniaturization and automation of the Cell Surface Capture (autoCSC) method, enabling sensitive and multiplexed interrogation of the surfaceome landscape of primary cells by direct identification of extracellular *N*-glycopeptides^{30,31}. On living cells, cell-surface carbohydrates are tagged with cell-impermeable biocytin-hydrazide. After cell lysis and tryptic digestion, glycopeptides are captured using streptavidin-filled tips using a process which is automated by using a liquid handling robot. After peptide:*N*-glycosidase F (PNGase F) treatment, which catalyzes the cleavage of asparagine-linked glycans, de-glycosylated peptides are eluted. This leaves a deamidation within the *N*-X-S/T consensus sequence of formerly *N*-glycosylated peptides, enabling specific identification of extracellular *N*-glycosylation sites and quantification of protein abundance with subcellular resolution by data-independent acquisition (DIA) mass spectrometry (MS)³². The main advantage of this chemoproteomic strategy focusing on

glycoproteins is the high surface specificity. CSC technology provides an accurate snapshot of the surface-residing pool and can discriminate surface proteins located in different intracellular compartments such as those located in secretory vesicles^{33–35}

Here, we performed a systematic quantitative proteotype analysis of the surfaceome during neuronal development and synapse formation using autoCSC. Bioinformatic analysis led to proteotype maps of the surfaceome in primary cortical cultures, which included about 1,000 extracellular *N*-glycoproteins. We also characterized dynamic, time-resolved surface protein abundance profile clusters that match developmental stage-specific patterns. Integrative data analysis revealed system-wide protein surface translocation in response to homeostatic plasticity and long-term potentiation and demonstrated that surfaceome protein abundance can be correlated or uncoupled from the total cellular abundance depending on the time resolution. Moreover, we found that differential changes in total protein abundance and surface-specific abundance are linked to subcellular organization. The resource and data shown indicate that localized proteotype maps are necessary in order to gain functional insights into spatiotemporal controlled biological processes, such as synapse formation, which are typically masked by broad omics-style approaches.

Results

Quantification of synapse numbers during development in culture

Primary neuronal cultures have been used to study fundamental aspects of neuronal development, synapse formation, and synaptic plasticity. Upon culture *in vitro*, neuronal cells synchronize and differentiate through well-defined stages into a network containing functional synapses^{11,36,37}. We first evaluated the time scale of synapse formation during neuronal development in cortical neuronal cultures. Cells were stained for synapsin to visualize presynaptic terminals, and staining for scaffolding proteins PSD95 and gephyrin was used to identify excitatory and inhibitory postsynaptic compartments respectively. The numbers of overlapping pre- and postsynaptic puncta were counted at 2-day intervals from 4 to 20 days *in vitro* (DIV) to quantify excitatory and inhibitory synapses (**Supplementary Fig. 1a**). Between 10 DIV and 18 DIV, excitatory and inhibitory synapse numbers increased more than 5-fold, followed by a slight reduction at 20 DIV (**Supplementary Fig. 1b**). Throughout this period, on average 72% of synapses were excitatory, with a standard deviation of 4% (**Supplementary Fig. 1b**). These data demonstrate that the majority of excitatory and inhibitory synapses form between 10 and 18 DIV; therefore this is the relevant time window for synapse formation in culture.

Quantitative analysis of the neuronal surfaceome during development

In order to quantify surfaceome dynamics during neuronal differentiation and synapse formation, we used autoCSC to take snapshots of the acute surface exposed *N*-glycoproteome every 2 days from 2 DIV to 20 DIV (**Fig. 1a**). For each time point we prepared three biological replicates of cortical cultures, originating from maximally four dishes for the earlier time points and minimally two cell culture dishes for the later time points per replicate. This accounted for expected variance in total protein mass over time in culture. We normalized the total peptide amounts in all replicates prior to automated *N*-glycopeptide capture. The eluted, formerly glycosylated and extracellular

peptides, were analyzed by DIA-MS and peptide-centric signal extraction, guided by a sample-specific spectral library^{32,38,39}. Overall, we identified 1,786 unique extracellular *N*-glycosylation sites (unique asparagines located within the N-X-S/T glycosylation motif within proteotypic peptides) and grouped them into 1,024 protein groups for quantification (**Supplementary Table 1**). We compared the identified sites with the UniProt database and found that 441 sites had been annotated previously while 1,345 sites were novel (**Supplementary Fig. 2, Supplementary Table 1**). For the 1,024 protein groups, we found numerous significantly enriched Gene Ontology (GO) annotations including plasma membrane localization (**Supplementary Fig. 3a**), receptor protein tyrosine kinase activity, receptor activity, ion channel activity, calcium binding (**Supplementary Fig. 3b**), cell adhesion, extracellular matrix, chemical synaptic transmission, and axon guidance (**Supplementary Fig. 3c**). For the majority of protein groups (76%) we obtained quantitative values for all time points. This overlap increased to 85% when the first two time points were excluded (**Fig. 1b**). These data provide a comprehensive picture of extracellular *N*-glycosylation sites and surfaceome proteins from primary cortical cultures. Furthermore, these results indicate that there are relatively few qualitative alterations to the surfaceome during maturation in culture, suggesting that regulation rather affects the quantitative surface abundance.

We first compared protein group quantities within replicates of the same time points and found high Pearson correlation coefficients with a median of 0.965 (standard deviation: 0.025) indicating high quantitative reproducibility (**Supplementary Fig. 4**). Next, we created a matrix of correlation coefficients comparing the protein group quantities at all time points (median among replicates) against each other (**Fig. 1c, Supplementary Table 1**). Between neighboring time points (e.g., 2 DIV vs. 4 DIV) we found generally high correlations (0.93 - 0.97). The lowest correlation coefficient of 0.73 was between the most distant time points (i.e., 2 DIV vs. 20 DIV). Comparing all time points with 20 DIV, we observed that the correlation gradually increased with decreasing distance to 20 DIV, reaching the midpoint at 6 DIV. Furthermore, we found lower correlations (0.82 - 0.94) among the earlier time points (2 to 8 DIV) compared to time points after 14 DIV (0.95 - 0.97) (**Fig. 1c**). This indicates that the majority of quantitative changes occur during the early phases of development, notably before peak synaptogenesis.

Next, we identified proteins with significantly different surface abundance levels compared to the preceding time point (fold-change > 1.5 and adj. p-value < 0.05) using pairwise testing. Across all comparisons we found 832 significant differences originating from 539 unique protein groups (**Supplementary Table 1**). The highest numbers of significant differences were found for the comparisons involving 4, 6, and 8 DIV (220,190, and 132 significantly different proteins, respectively). In contrast, for 16, 18, and 20 DIV only 41, 34, and 39 proteins had modulated surface abundance, respectively (**Supplementary Table 1, Supplementary Fig. 5**). This demonstrates that there is substantial remodeling of the neuronal surface (>50% of all measured proteins) during differentiation in culture, with the most quantitative protein surface abundance changes occurring during the early stages. Notably, most surface protein abundance changes occurred prior to the time window for synapse formation, and few changes were observed after 10 DIV.

Surface-abundance profiles reveal developmental stage-specific patterns

In order to investigate the diversity in surface abundance profiles over time, we used unsupervised fuzzy clustering of all proteins identified in at least seven time points⁴⁰. Using the minimum centroid distance to determine optimal number of clusters (**Supplementary Fig. 6**)⁴¹, we obtained six clusters with characteristic surface-abundance profiles (**Fig. 2a, Supplementary Table 1**). Clusters 1 and 4 include proteins that increased or decreased in abundances, respectively. Cluster 2 proteins increased in surface abundance across the time course, but had an initially steeper abundance increase compared to proteins in cluster 1. Clusters 3, 5, and 6 featured dynamic profiles with alternating directionality.

To determine whether annotations of the protein group clusters reflect functional requirements of specific developmental stages, we retrieved ontology annotation data for the proteins of each cluster and selected significantly enriched annotations ($p < 0.05$) that showed specific enrichment in one cluster (**Fig. 2b**). The abundances of cluster 2 proteins steeply increased in abundance until 8 DIV and had relatively stable abundances afterward. Interestingly, we found specific enrichment of the terms “synapse assembly” and “regulation of synapse assembly” for cluster 2, indicating that synapse assembly factors reach the maximum surface abundance several days before the onset of synapse formation (**Supplementary Fig. 1b**). Cluster 1 proteins increased in abundance starting at around 4 DIV and reached a plateau at around 16 DIV. Terms associated with synapse localization (e.g., “postsynapse”, “presynapse”, “glutamatergic synapse”) and synaptic function (e.g., “synaptic signaling”, “chemical synaptic transmission”, “ion channel activity”, “neurotransmitter receptor activity”, “regulation of membrane potential”) were specifically enriched in cluster 1 (**Fig. 2b**). This indicates that synaptic proteins in general are increasingly trafficked to the cell surface days before the majority of synapse formation takes place. Furthermore, we found that abundances of cluster 1 proteins reach the maximum surface intensity at 16 DIV, whereas synapse counts continued to increase until 18 DIV (**Supplementary Fig. 1b**). Cluster 5 proteins also had increasing surface abundance at early time points, reaching a peak at 6 to 8 DIV, followed by a continuous decrease through 20 DIV (**Fig. 2a**). This raised the question whether proteins in this cluster have functions associated with the period at the cluster peak. DIV 5 to 8 is the period associated with outgrowth and branching of dendrites^{21,36,37}. Indeed, we found enrichment of proteins involved in cell projection (terms: “cell projection organization”, “plasma membrane bounded cell projection”, “cell projection morphogenesis”) as well as “chemorepellent activity” and “semaphorin receptor binding” for proteins of cluster 5. Cluster 4 protein abundances continuously decrease over time and are associated with terms such as “cell migration”, “growth factor binding”, and “focal adhesion”. Potentially these proteins are of importance during the initial 48 hours in culture. Clusters 3 and 6 share a curious feature: Both show an acute increase in abundance starting at 12 DIV (**Fig. 2a**), the time point when synapse formation increases considerably (**Supplementary Fig. 1b**). Interestingly, both clusters are enriched in proteins associated with intracellular membranes, but the two clusters are enriched in membranes from different organelles (cluster 3: “endoplasmic reticulum part”, “membrane enclosed lumen”, cluster 6: “vacuolar membrane”, “lysosomal membrane”, “coated vesicle”). These intracellular membranes potentially appear at the surface at increased rates due to alterations in surface trafficking. Associated annotations point to functions related to degradation or clearing of biomolecules from the surface (cluster 3: “proteolysis in cellular catabolic process”, “ERAD

Pathway”, cluster 6: “catabolic process”, “autophagy”, “hydrolase activity”) but also synthesis of new biomolecules (cluster 3: “glycoprotein biosynthetic process”, “macromolecules biosynthetic process”) (**Fig. 2b**). These findings could reflect acute changes in the dynamic interplay of biosynthesis, endosomal degradation, recycling, and surface trafficking, all important for control of synapse formation and modulation of synaptic plasticity^{11,42–44}. Altogether, these data illustrate distinct and dynamic surface-abundance profile clusters that reflect stage-specific functional requirements during neuronal development. Furthermore, the data indicate that synapse assembly factors and synaptic proteins are produced and trafficked to the neuronal surface prior to the onset of synapse formation in culture.

The *in silico* neuronal surfaceome interaction network

The cluster analysis suggested that functionally related proteins have similar surface-abundance profiles during neuronal development in culture. The closest form of relationship on the molecular level is arguably direct physical interaction and formation of a protein complex. Therefore, we asked whether known protein complexes have higher correlations in surface-abundance profiles across our time series. We calculated Spearman correlation coefficients of the surface abundances for all pairwise combinations of surface proteins. We found an approximately symmetric distribution with a median of 0.04, indicating no correlation on average. Next, we evaluated pairs of proteins known to be in a complex together⁴⁵ and found that 83% were in the positive range with a median correlation coefficient of 0.55 (**Supplementary Fig. 7**). Despite the positive correlation for protein complexes in this system-wide analysis, we also found examples of interacting proteins with low or even negative correlations.

In order to provide a bird's-eye perspective on surfaceome connectivity, we created a map of the surfaceome, associated interactions, and developmental surface profiles (**Fig. 3a,b**) using interaction data obtained from the STRING database. For a more in-depth analysis of specific proteins of particular interest, we first mapped ligand-gated ion channels (**Fig. 3c**)⁴⁶, consisting of glutamate and GABA receptor complexes. More than half of ligand-gated ion channels were grouped into cluster 1; almost three-quarters of ligand-gated ion channels belong to either cluster 1 or cluster 2 (**Fig. 3d**). Receptor subunits matching outside of the majority clusters could indicate a modulatory function of the receptor or subunit exchange during neuronal development. For example, GABA-A receptor complex subunits are spread over 4 different clusters, reflecting underlying molecular and functional heterogeneity⁴⁷. Next, we mapped trans-synaptic cell adhesion molecules⁴⁶ to the surfaceome network (**Supplementary Fig. 8a**). This analysis revealed several subnetworks. For example, the ephrin family is primarily associated with clusters 4 and 5 and cadherins are mostly associated with clusters 1 and 2. Cell adhesion molecules are relatively underrepresented in clusters 3 and 6, which involve proteins that increase in abundance starting at 12 DIV. This supports the notion that surface expression of cell adhesion molecules does not increase during synapse formation or synaptic activity.

Finally, we examined proteins encoded by mRNAs that are enriched in neurons compared to astrocytes or vice versa. Since cortical neuronal cultures are mixed neuron and astrocyte cultures, this comparison could inform on the cell type of origin for a number of surface proteins. From cell-type resolved RNA-seq data⁴⁸ we selected protein groups matching transcripts that are enriched

5-fold or more in one cell type compared to the other (**Supplementary Fig. 8b-c**). Proteins from clusters 3 and 6 are encoded by mRNAs more highly expressed in neurons than in astrocytes, whereas mRNAs that encode cluster 4 and 5 proteins are enriched in astrocytes. Interestingly, some subnetworks feature surface proteins from both cell types, for example the ephrins and semaphorins, potentially hinting at inter-cell type molecular interactions. In summary, this map of the neuronal surfaceome reveals connectivity and developmental dynamics and will be a comprehensive resource for the neuroscience community.

Differential regulation of surface and total cellular pools

A dynamic interplay of biosynthesis, surface trafficking, and endosomal degradation and recycling provides the cell surface with the necessary quantity of adhesion molecules, neurotransmitter receptors, ion-channels, and other factors required for neuron development and synaptic plasticity⁴⁴. In order to investigate this dynamic process, we subdivided cell surface proteins into two theoretical pools: a total pool comprised of proteins present at the surface and intracellularly, and the surface pool as measured by autoCSC. Comparison of these pools would enable investigation of different levels of organizational principles: for example, whether observed changes in surface abundance are explained by changes in the total protein abundance or by altered surface trafficking. In order to obtain data on the total pool, we performed proteotype analysis on the same samples described above by measuring the non-*N*-glycosylated tryptic peptides by DIA-MS (**Fig. 4a**)^{32,38,39}.

In total, we quantified approximately 7,400 protein groups and identified significantly differentially expressed proteins (fold-change > 1.5 and adj. p-value < 0.05) using pairwise testing against the preceding time point as in autoCSC (**Supplementary Table 2**). Across all comparisons we found 3,061 significant differences matching 2,193 unique protein groups (**Supplementary Fig. 5**). Thus, about 30% of the measured proteome is differentially expressed across the time course of neuronal differentiation (**Supplementary Table 2**). This finding is in line with Frese et al. who reported remodeling of one-third of the neuronal proteotype in a similar experiment¹¹. By comparison to the autoCSC data, we found that the neuronal surfaceome is more dynamic than the total proteome. About 53% of surfaceome proteins were differentially regulated in the pairwise comparisons over time. The total abundance is determined by the interplay of protein synthesis and degradation, and regulated surface trafficking likely accounts for the higher extent of differential expression on the surface.

For a more direct comparison, we matched protein groups from the surface and total pool; information on both pools was available for about 650 protein groups (**Supplementary Table 2**). Since the quantitative values from each of the pools originate from different peptides, we cannot directly compare surface with total abundance for individual proteins. We can however, compare the abundance changes across the time series of neuronal development between the surface and total pool. In order to determine whether the total protein abundance for a surface protein reflects the surface abundance, we performed a number of complementary analyses. First, we asked whether the protein abundance profiles across the time course of neuronal development correlate between surface and total pools. We calculated Spearman correlation coefficients for each protein and found that 78% had a positive value with a median correlation coefficient of 0.48, indicating

a strong positive correlation for the majority of surface proteins across the neurodevelopmental time course (**Fig. 4b, Supplementary Table 2**). Thus, over the entire time course of 20 days, the total abundance profile reflects the surface abundance for many proteins.

The relevant time scale for modulation on the level of surface trafficking might be shorter than the 18-day interval evaluated. In order to investigate the relationship of surface and total abundances over time, we calculated pairwise comparisons between time points. This resulted in 45 comparisons for both the surface and total abundance pools (**Supplementary Table 2**). First, we compared the abundance changes between the two most distant time points, 2 DIV and 20 DIV, and visualized them in a scatterplot (**Supplementary Fig. 9**). Proteins in the top right quadrant are more abundant at 20 DIV for both surface and total pools. Likewise, proteins in the bottom left quadrant are less abundant at 20 DIV for surface and total pools. Proteins in quadrants 2 and 4 show disagreement in their abundance change. The majority, 82%, of all significantly regulated proteins have agreeing directionality (i.e., they were found in quadrants 1 and 3) (**Supplementary Fig. 9**). Furthermore, we found a 43% overlap of significantly different proteins and a correlation coefficient of 0.73 for the comparison between the most distant time points (**Fig. 4c-d**). Next, we asked how these parameters change when the time window of observation was decreased. Interestingly, the median correlation coefficient decreased with decreasing time between measurements, to a median of 0.26 for neighboring time points (**Fig. 4c**). Similarly, the overlap of significantly different proteins between surface and total pools decreased from 43% to 13% with decreasing time between compared measurements (**Fig. 4d**). Together, this demonstrates that for many proteins the total abundance pool correlates with the surface pool over the entire time course of neuronal differentiation in culture but there are considerable fluctuations over time. These findings suggest that changes in surface trafficking influence surface abundance generally on short time scales, whereas total protein abundance modulates the surfaceome over long time periods.

Functional implications of uncoupling of surface and total abundance

If surface and total abundance of a protein are highly correlated, there is likely little regulation of surface trafficking. Conversely, if surface and total abundance are uncoupled, there is presumably systematic modulation of surface abundance by differential trafficking. Identifying proteins with the most variation between surface and total abundance might therefore shed light on protein function. Therefore, we sought to systematically identify the proteins with the most deviation between surface and total abundance during neurodevelopment in culture. Proteins in the previously described protein clusters (**Fig. 2a**) generally had temporal responses that fit an impulse model; this is a parametric model with an early response followed by a second transition to a steady state⁴⁹. Using impulse models⁵⁰ to model our time series data we observed very good agreement between modeled surface and total abundance profiles for many proteins (**Supplementary Figure 10**). This suggests that for these proteins in this particular experimental setup, changes in surface abundance are predominantly determined by the total abundance, without detectable regulation on the level of surface trafficking. For 128 proteins we observed differential regulation (adj. p-value < 0.01, **Supplementary Table 2**). Interestingly, synaptic vesicle proteins SV2a and SV2b were among the significantly regulated proteins. Synaptic

vesicles are assembled intracellularly and only become surface exposed once exocytosis is increased during synapse formation and initialization of synaptic activity. There was a continuous increase in total abundance of SV2a and SV2b beginning early in development. Amounts in the surface pools, however, did not change until the onset of synapse formation (12 DIV), and then we observed significant increases in surface abundance that reached steady state at the late time points (**Fig. 4e-f**). Furthermore, we found similar profiles for Slc6a17, Ggt7, and the neuronal pentraxin receptor Nptxr⁵¹ (**Fig. 4 g-i**). In summary, these data show that differences between regulation of surface and total abundance can reflect protein function and subcellular organization.

Homeostatic plasticity induces reorganization of the neuronal surfaceome

Changes in synaptic strength are referred to as synaptic plasticity and thought to underlie learning and memory formation. Different forms of plasticity have been described. Long-term potentiation (LTP) acts on individual synapses and is characterized by a long-lasting increase in synaptic strength upon high-frequency stimulation^{2,3,52}. In contrast, homeostatic plasticity, or synaptic scaling, can affect the strengths of multiple synapses proportionally, potentially promoting network stability⁵³. We asked how the quantitative composition of the neuronal surfaceome adapts in response to LTP and synaptic scaling. LTP is typically measured over a time scale of minutes, whereas homeostatic plasticity is measured over days.

To investigate homeostatic plasticity, we elicited synaptic up- and downscaling in cortical neuronal cultures (DIV 21) by treatment with the neurotoxin tetrodotoxin (TTX, 1 μ M) or with the GABA-A receptor antagonist bicuculline (BIC, 40 μ M), respectively, for 24 hours. Samples were analyzed by autoCSC (**Fig. 5a**). As surface SV2a and SV2b levels increased with synapse formation and neuronal activity, we expected to observe a decrease in surface abundance upon TTX treatment. Indeed, there was a significant reduction of both SV2a and SV2b compared with untreated controls (**Fig. 5b,c**), indicating a net decrease of neuronal synaptic vesicle release. In contrast, upon downscaling of GABAergic neurotransmission using BIC, which leads to onset of rapid neuronal firing, there was a significant increase in surface SV2a and SV2b (**Fig. 5b,c**), suggesting neuronal firing events lead to a net increase in synaptic vesicle fusion events. These results agree with previous findings that homeostatic synaptic scaling predominantly influences the postsynapse rather than presynaptic vesicle release and recycling⁵⁴.

During synaptic scaling, as during neuronal development, the qualitative surfaceome composition did not significantly change. Overall, we quantified 864 protein groups, with 850 identified in all conditions. In a quantitative analysis, 246 proteins were significantly different (fold-change > 1.5 and adj. p-value < 0.05) compared to an untreated control (**Fig. 5d, Supplementary Table 3**), indicating extensive quantitative remodeling of the neuronal surface. Of these, the levels of 102 proteins were changed in both up- and downscaling with coordinate directionality. This indicates a role in a general response to global changes in neuronal activity, regardless of the sign of plasticity (**Fig. 5d**). An analogous observation was reported by Schanzenbächer et al.: These authors found a similar proportion of the newly synthesized proteome with consistently enhanced or reduced synthesis for both up- and down-scaling^{12,13}. Functional annotation analysis of all regulated proteins revealed significant enrichment in terms related to synaptic function (e.g.,

“sodium channel activity”, “transmembrane receptor kinase activity”, “membrane depolarization”, “action potential”). Interestingly, the vast majority of proteins associated with an enriched term had positive fold-change and agreement in directionality between opposite scaling paradigms (**Supplementary Fig. 11**).

Previous studies have mechanistically linked calcium influx with synaptic upscaling^{55,56}. In support of this, we found that surface abundances of a number of voltage-gated calcium channels were significantly modulated in response to both homeostatic plasticity paradigms (e.g., *Cacna2d3*, *Cacna1d*) or only to downscaling (e.g., *Cacna1c*) (**Fig. 5d**). *EphA4* has been shown to mediate synaptic downscaling⁵⁷, and we observed a significant increase in levels of this protein upon both up- and down-scaling (**Fig. 5d**). To specifically investigate proteins with bi-directional regulation comparing TTX with BIC treatment, we performed significance testing and identified 68 proteins with differential abundance (**Fig. 5e, Supplementary Table 3**). Most of these proteins either increased in surface abundance during upscaling and decreased in surface abundance after downscaling or vice versa, indicating that the change was opposite the polarity of stimulation. Interestingly, both receptor-type tyrosine-protein phosphatase-like proteins *Ptprn* and *Ptprn2* changed in surface abundance upon synaptic scaling (**Fig. 5e**), suggesting a role in this process. Although *Ptprn* does not change upon upscaling, it significantly increased in surface abundance upon downscaling. The opposite was true for *Ptprn2*, as we observed no change during downscaling but a decreased surface abundance in response to TTX (**Fig. 5e**).

Similarly, we observed remarkable and unique differential regulation for the three neuronal pentraxins *Nptx1*, *Nptx2*, and *Nptxr* (**Fig. 5e**). *Nptxr* was less abundant on the surface after upscaling and more abundant after downscaling. Upscaling elicited no change in *Nptx2* surface abundance, but downscaling led to a significant increase in surface abundance. *Nptx1* increased in surface abundance upon both up- and downscaling (**Fig. 5e**). In agreement with our data, it was previously reported that surface abundance of *Nptx1* increases after 24 hours of TTX treatment and that inhibition of *Nptx1* expression blocks synaptic upscaling⁵⁶.

We did not detect significant changes in any condition for any subunit of the AMPA receptor (**Fig. 5e**). However, three metabotropic glutamate receptors had significantly polarized responses. *Grm1*, *Grm4*, and *Grm5* had different responses to upscaling than to and downscaling, predominantly due to lower surface abundance upon BIC treatment (**Fig. 5e**). Finally, we identified two related proteins, *Sidt1* and *Sidt2*, with strong and different responses to synaptic scaling. *Sidt1* abundance increased upon upscaling but decreased after BIC treatment. In contrast, *Sidt2* abundance decreased in both conditions, albeit significantly more strongly during downscaling (**Fig. 5e**). These findings suggest a connection between synaptic plasticity and cellular transfer of RNA as *Sidt1* and *Sidt2* bind and transport double-stranded RNA^{58,59}.

Next, we asked whether the changes we observed on the neuronal surface were reflected in the total proteotype. Across all comparisons, 28% of all quantified surface proteins changed in abundance, compared to 8% for the total proteome, further supporting our finding that the surfaceome is more dynamic than the total proteome (**Supplementary Table 3**). Only 2% of the changes in surface abundance were accompanied by a significant change of the same proteins

in total abundance after 24 h (**Fig. 5f, Supplementary Table 3**). We also noted that the surface proteins that changed in abundance, the fold-change difference was higher for the surface abundance change than for the total abundance change (**Supplementary Fig. 12**). This further demonstrates that the surfaceome is more dynamic and flexible than the total proteome, a characteristic necessary for achieving a homeostatic response. For the few surface proteins that increased both on surface and total abundance, we found agreement with previous reports. During synaptic upscaling total and surface abundance levels of Nptx1 increased (**Fig. 5e**), which recapitulates previous findings achieved with orthogonal approaches⁵⁶. For synaptic downscaling, our data on Nptx2 (**Fig. 5f**), provided supporting evidence for polarized roles of neuronal pentraxins in homeostatic plasticity. Together, these results provide a comprehensive picture of dynamic surfaceome changes in response to homeostatic plasticity, recapitulating previous knowledge, and revealing new opportunities for in-depth functional investigation. Importantly, the data indicate that there is dynamic reorganization of the neuronal surface during synaptic scaling that is largely independent of global protein abundance change.

Surface trafficking of diverse cargo during LTP

NMDA receptor-dependent long-term potentiation (LTP) is a well-studied form of synaptic plasticity, and there is a mechanistic understanding of early molecular events, prominently involving the modulation of synaptic AMPA receptor synaptic abundance and post-translational modifications^{3,52}. One hallmark of LTP is surface insertion of AMPA receptors from intracellular pools, and an intact exocytosis machinery is crucial for LTP⁶⁰. A three-step model for AMPA receptor synaptic retention has been proposed that involves exocytosis at extra/perisynaptic sites, lateral diffusion to synapses, and a subsequent rate-limiting diffusional trapping step⁶¹. Although evidence for the importance of surface diffusion is accumulating^{62–64}, the role of AMPA receptors for the dependence of LTP on exocytosis has not been fully clarified, and there is speculation that currently unrecognized cargo are also essential for LTP^{65,66}. For a discovery-driven and comprehensive analysis of surfaceome changes in response to LTP, we elicited cLTP in cortical cultures at DIV 14 followed by autoCSC surfaceome analysis 20 min later (**Fig. 6a**). As expected, we found that Gria1 and Gria2 had significantly increased surface abundance upon stimulation (**Fig. 6b, c**) indicating that the cLTP protocol triggers AMPA receptor exocytosis. Gria3 abundance was increased on the neuronal surface as well; although the effect reached statistical significance (**Fig. 6d**), it was slightly above the threshold after FDR-adjustment of p-values (**Fig. 6e, Supplementary Table 4**). Interestingly, there was a strong increase in surface abundance for AMPA auxiliary subunit stargazin (also known as Cacng2) (**Fig. 6e**); this subunit promotes delivery of the AMPA receptor to the surface. Furthermore, stargazin is well-known for its ability to trap AMPA receptors at synaptic sites by direct interaction with PSD95^{61,67}. In addition to AMPA receptor subunits, we identified 36 surface proteins that were significantly increased in abundance and four that were reduced in surface abundance after cLTP (**Fig. 6f**). Three enriched proteins had been previously connected to LTP by studies investigating their loss-of-function: Wnt-5a, the major prion protein Prnp, and the adenylate cyclase Adcy3. Inhibition of expression of any of these proteins leads to functional LTP defects^{68–70}. The strongest responder was the receptor-type tyrosine-protein phosphatase Ptpn (**Fig. 6f**), which is removed from the surface in response to cLTP (**Fig. 6f**). Interestingly, we found that Ptpn levels were increased on the surface during synaptic downscaling. These results suggest that Ptpn has a role in negative regulation of

synaptic strength. In contrast, we observed increased exocytosis for another receptor-type tyrosine-protein phosphatase, Ptpcr.

We grouped the proteins with significantly different surface abundances after cLTP and visualized their interaction network (**Fig. 6g**). This visualization illustrates that, in addition to the AMPA receptor subunits and stargazin, three ion channels and ten other receptors increased in surface abundance upon cLTP. We identified receptors from both pre- and post-synaptic sites (e.g., adenosine receptor A1 and cannabinoid receptor 1) and of various neurotransmitter types. The majority of receptors identified are postsynaptic G-protein coupled receptors (i.e., adhesion G protein-coupled receptor B1, D(1A) dopamine receptor, 5-hydroxytryptamine receptor 2C, muscarinic acetylcholine receptor M4, and alpha-2A adrenergic receptor) and interact with second messenger Adcy3, which was also increased in abundance. In addition to receptors, ten secreted proteins significantly changed in abundance, including semaphorin-3A, bone morphogenetic protein 3, and IgLON family member 5. Furthermore, four adhesion molecules, two solute carriers, two tetraspanins, and seven proteins with miscellaneous functions had altered abundance upon cLTP (**Fig. 6g**). Some of the identified proteins suggest links between LTP and cellular processes that had not previously been associated with LTP. For example, Tmem110, which was trafficked to the surface upon cLTP, and was recently shown to regulate store-operated calcium entry at junctions that spatially connect the plasma membrane with the endoplasmic reticulum⁷¹. Furthermore, the increased abundance of volume-regulated anion channel subunit Lrrc8b, which plays a central role in the maintenance of cell volume, potentially provides a link between early LTP and structural plasticity of dendritic spines^{72,73}. The narrow time window for cLTP makes it unlikely that any of the observed increases on the surface are due to changes in total abundance of these proteins; however, specific degradation of surface proteins might occur concurrently with endocytosis. Therefore, we analyzed the total proteotype as before and found no proteins with significantly increased abundance (**Supplementary Table 4**). We did, however, identify proteins with reduced total abundance after cLTP, potentially due to rapid degradation. These proteins are mostly cytosolic, and we found no overlap with the identified surface proteins that decreased in surface abundance after cLTP (**Supplementary Fig. 13**). We validated the results from autoCSC using an orthogonal methodology, namely neuro-morphology. Guided by the availability of commercial antibodies suitable for live cell imaging, we selected three proteins for live-cell surface labeling. We confirmed the increased surface abundance using immunocytochemistry for the AMPA receptor, Bai1 and Adcy2 after cLTP in primary cortical neurons (**Fig. 6h,i**). Both Bai1 and Adc3 showed a significant increase in mean fluorescence intensity on principal dendrites after cLTP, in line with the results from autoCSC (**Fig. 6h,i**). For Adcy3 we additionally observed localization to synaptic sites, identified by puncta overlapping with presynaptic marker synapsin 1/2 (**Supplementary Fig. 14**). These data illustrate the diverse adaptations on the neuronal surface that occur in addition to alterations in AMPA receptor trafficking during LTP. The identified molecules provide a number of avenues to investigate the molecular mechanisms underlying the dependency of LTP on exocytosis.

Discussion

A comprehensive overview of how molecular dynamics at synapses enable construction and plasticity of neuronal circuits has been elusive. The vast number of proteoforms that contribute to different processes in parallel, with generally unclear interdependencies, gives rise to a complexity that has been beyond comprehension^{6,7,52,65,74}. Furthermore, cells are capable of elaborate computations, even for reductionist model systems and isolated molecular events^{8,75}, raising the possibility that bioinformatic models and analyses will be required to decipher non-trivial relationships. To implement such modeling, detailed knowledge about all molecules involved, their mechanisms of action and their interplay with appropriate spatial and temporal resolution is required. Targeted genetic manipulation and/or molecular biology combined with phenotypic measurements of synaptic structure and properties can provide in-depth information regarding the function, localization, and post-translational modifications of individual molecules, but this requires prior knowledge and a focus on a few genes of interest. Discovery-driven and system-wide approaches can inform on many molecules, but the measurement of global RNA or even protein abundance levels are an abstraction of the actual process of interest: the activity of a particular protein in executing a particular spatiotemporally designated function. While there is no suitable all-in-one solution available, integration of different types of data will be required. Here, we used a time-resolved spatial chemoproteomics approach to evaluate neuronal development and synaptic plasticity. We used this approach to (i) map proteins at a defined subcellular structure, the surface, in a discovery-driven fashion, (ii) to perform system-wide quantification of both surface and total cellular abundance, and (iii) to quantify subcellular of distinct cellular protein pools.

Here, we present an initial blueprint of how many, and which, proteins are present on the surface of neurons. First, neurons come in different populations and our rat cortical neuronal culture system contains a mixture of these cells. Furthermore, our cultures contain predominantly neurons, but also astrocytes. We addressed this question partially by use of transcriptomic data; a more complete delineation could be achieved by combination with cell-type specific metabolic labeling approaches^{10,76}. From a methodological point of view, there are two major biases in our analysis. First, our approach is limited to proteins with extracellular *N*-glycosylation. It is well established that *N*-glycosylation is a common feature among surface proteins⁷⁷ and more than 95% of cell surface proteins have an extracellular glycosylation motif⁷⁸. Nevertheless, there are proteins with important surface functions, for example AMPA auxiliary subunits^{22,79}, that are not glycosylated and thus were not considered here. More crucially, we only identified *N*-glycosylated sites if they were present within a tryptic peptide that is proteotypic (after protein grouping) and suitable for MS analysis, which depends on biophysical properties such as peptide length. Although we calculated that a large proportion of *N*-glycosylation sites are located within proteotypic peptides after tryptic digestion (>90% for mouse and human *N*-glycosylation sites in Uniprot), the percentage of resulting peptides that are detected by MS is more difficult to assess. We can grossly approximate the number of missed *N*-glycoproteins by extrapolation from the percentage of missed additional glycosylation sites for proteins with confirmed presence by autoCSC. For a comparable autoCSC dataset with human cells³⁰, we calculated the percentage of missed glycosylation sites (retrieved from Uniprot) in the range of two-thirds of all potentially present *N*-glycosites. Assuming two *N*-glycosites per surface protein on average, we estimate

that about one-third of surface proteins were not detected. This suggests an approximate size of 1500 proteins for the cortical neuronal culture surfaceome. We provide experimental evidence for 1,786 unique extracellular *N*-glycosylation sites. Of these, as shown by comparison with Uniprot, 1,345 were not previously described. It should be noted that annotation for rat proteins is considerably less comprehensive than for human or mouse.

We observed very few qualitative differences on the surface during neuronal development in culture, which is rather surprising considering the profound morphological changes that cells undergo during this process³⁶. In contrast, the quantitative analysis of neuronal surfaceome dynamics revealed substantial remodeling of the surface during development. Most of the differences were observed within the first week, which is the time period of the most drastic morphological changes³⁶. We used unbiased clustering of protein abundance profiles to reveal developmental-stage-specific patterns. These data indicate that the acute functional requirements imposed on the neuronal surface are reflected in the quantitative surfaceome composition. Comparing the surface proteotype data with synapse counts along the developmental time series, we showed that the cluster enriched for synapse assembly proteins had a maximum surface abundance at 8 DIV, four days before the increase of synapse counts. Furthermore, proteins in the cluster enriched with synaptic proteins are present on the surface at the time when synapse counts begin to increase, and synaptic proteins reached peak abundance 2 days before the peak of synapse counts at 18 DIV. In a total proteotype analysis, Frese et al. found identical early dynamics of synaptic proteins¹¹. Similarly, *in vivo* single-cell transcriptomic analysis of newborn cortical neurons revealed that 12-hour old neurons express transcripts of synaptic genes⁸⁰. Together, this suggests that many synaptic proteins are produced and trafficked to the surface before synapses are formed and only later are these proteins organized into synaptic microdomains by surface diffusion. The existence of such a mechanism has been proposed based upon the finding that basic circuit connectivity, including dendrites and spines, can be formed in the absence of presynaptic glutamate release⁸¹. Synaptic components may be trafficked to the surface before synapses are formed to allow rapid adaptation and modification of cell-surface microdomains in response to external stimuli. For example, glutamate triggers *de novo* spine growth from the dendrite shaft via NMDA receptors within merely 20 seconds⁸². Similar results were also found in cells treated with GABA and GABA_A receptors (GABA_ARs)⁸³. This rapid response could only be possible if proteins were present at the surface at the onset of stimulation.

Comparing the total pool with the surface abundance pool during neuronal development and synaptic plasticity, we investigated the interplay of surface trafficking and total abundance change on a system-wide scale. We found that the surfaceome is more dynamic than the total proteome as indicated by the percentage of proteins that underwent significant changes during the 20 days of culture. When synaptic transmission was scaled as homeostatic mechanisms after treatment with TTX or BIC, we found that the fold-change difference compared to untreated controls was significantly higher for the surface compared to the total abundance pool. Across the 20 days of culturing, surface and total levels for many proteins had high correlation, suggesting that the surface abundance is predominantly determined by the total abundance. However, when we compared neighboring time points with 2 days between measurements, the correlation and overlap of significantly modulated surface proteins was decreased. These findings suggest that

total protein abundance modulates the surfaceome on a broad scale over a long time period, whereas changes in surface trafficking are more pronounced at smaller time scales. The data also suggest that due to the level of regulation by surface trafficking, the surfaceome is more flexible and can achieve a higher dynamic range of protein quantities during a limited time window, as exemplified during homeostatic scaling.

Furthermore, the uncoupling of surface and total abundance changes has functional implications. For synaptic vesicle membrane proteins, we detected the assembly of intracellular pools that increasingly became surface exposed upon synaptic activity. We were able to dissect and identify differential surface trafficking with the autoCSC method; however, synaptic vesicle pools represent an extreme case in biology that exploits intracellular vesicle pools and tightly controlled exocytosis, and these pools are readily detected. We also identified unique differential regulation for the neuronal pentraxin receptor, potentially indicative of intracellular accumulation. Although neuronal pentraxins interact with AMPA receptors, we did not observe AMPA receptor surface abundance modulation during homeostatic plasticity. Previous reports have shown increased synaptic transmission that involves AMPA receptors occurs after 24 hours of TTX treatment^{13,54,55}. This could occur, however, without modulation of global AMPA receptor surface abundance by surface diffusion leading to synaptic accumulation or post-translational modifications of the receptor. In support of this hypothesis, Diering et al. found no significant changes for Gria1, Gria2, or Gria3 surface abundance after 24 hours of TTX treatment, in agreement with our findings. They observed reduced Gria1 and Gria3 surface abundance after 24 hours of BIC treatment, whereas our experiments did not recapitulate this observation⁸⁴. A potential explanation for this difference could be the age of culture prior to cLTP experiments. For homeostatic plasticity experiments we used mature 21 DIV cultures, whereas Diering et al. used 13-15 DIV cultures that presumably contained more immature synapses. The considerable increase in synapse counts during this time period might account for the observed differences. Considering that neuronal pentraxins are known to cluster AMPA receptors, our data argues for a role of AMPA receptor clustering, rather than surface trafficking in the first 24 hours of synaptic upscaling. Furthermore, our findings suggest a number of new avenues for investigation in homeostatic plasticity as our data suggest that double-stranded RNA transporters Sidt1 and Sidt2 and metabotropic glutamate receptors Grm1, Grm4, and Grm5 are involved. Notably, we also observed overlap between LTP and synaptic scaling: Ptpn increased in surface abundance during synaptic downscaling and decreased abundance after cLTP.

Synaptic recruitment of AMPA receptors from extrasynaptic pools by surface diffusion is required for LTP⁶². Considering the basal extrasynaptic reserve pool of AMPA receptors, the question has been raised whether exocytosis of new AMPA receptors is needed for early LTP or whether other cargo mediates the strict requirement of exocytosis for LTP⁶⁵. Our data provides support for the second hypothesis. First, we identified numerous proteins that were exocytosed upon cLTP, and these factors could account for the necessity of exocytosis. Second, we observed a strong increase in abundance of AMPA auxiliary subunit stargazin, which has been shown to mediate synaptic trapping of AMPA receptors by direct interaction with PSD95⁶¹. Based on these results we hypothesize that increased surface delivery of stargazin shifts the dynamic equilibrium between extrasynaptic and synaptic AMPA receptors to promote diffusional trapping of mobilized

AMPA receptors, thereby connecting the requirement for exocytosis with surface diffusion and synaptic trapping.

In conclusion, we performed a quantitative analysis of neuronal surfaceome dynamics during synapse formation and synaptic plasticity with unprecedented depth using the recently miniaturized and automated method that we call auto CSC. The experiments described here revealed the widespread importance of modulation of the surfaceome on the level of surface trafficking. The comprehensiveness of our resource enabled insights into principles and organization of the neuronal surface proteotype, and the data collected suggest avenues for further in-depth exploration.

Figure 1

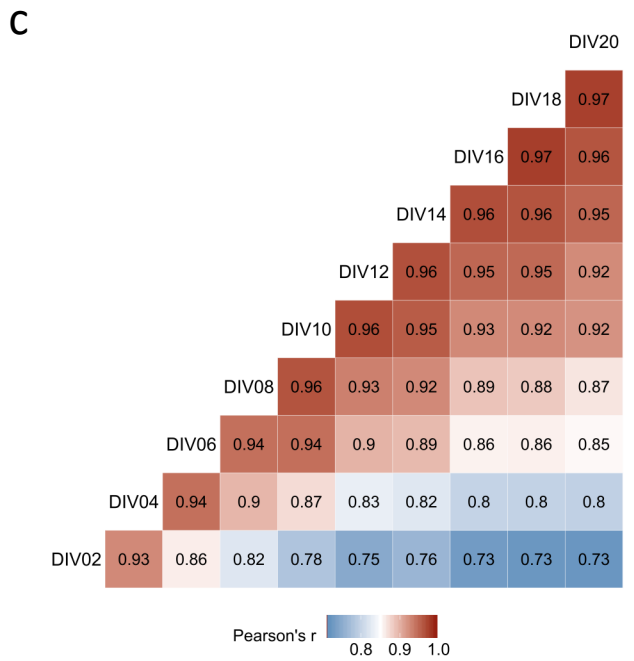
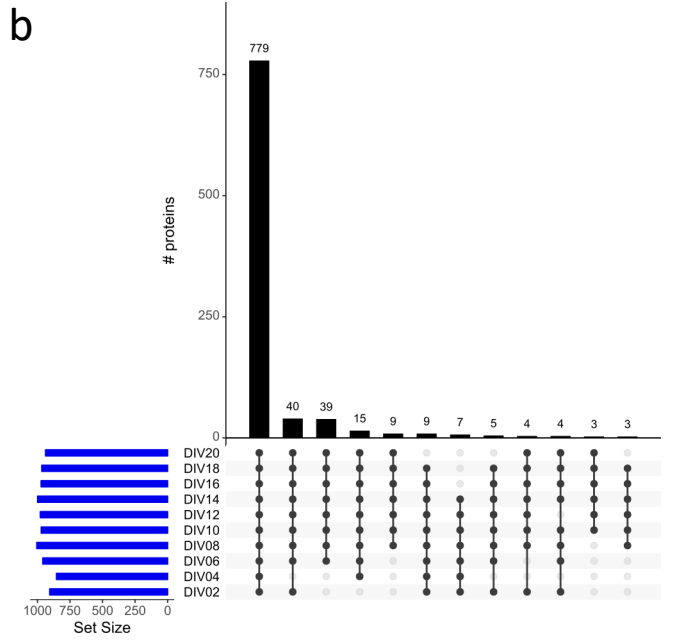
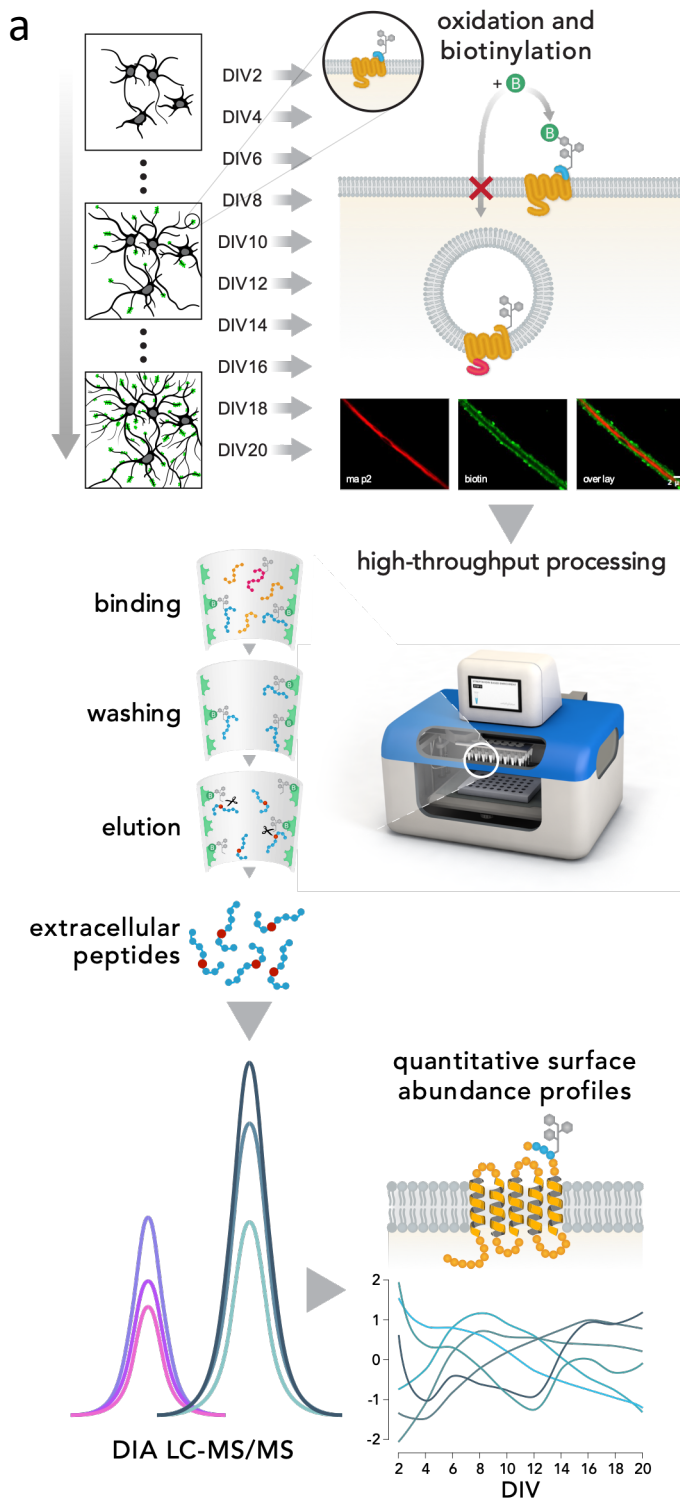
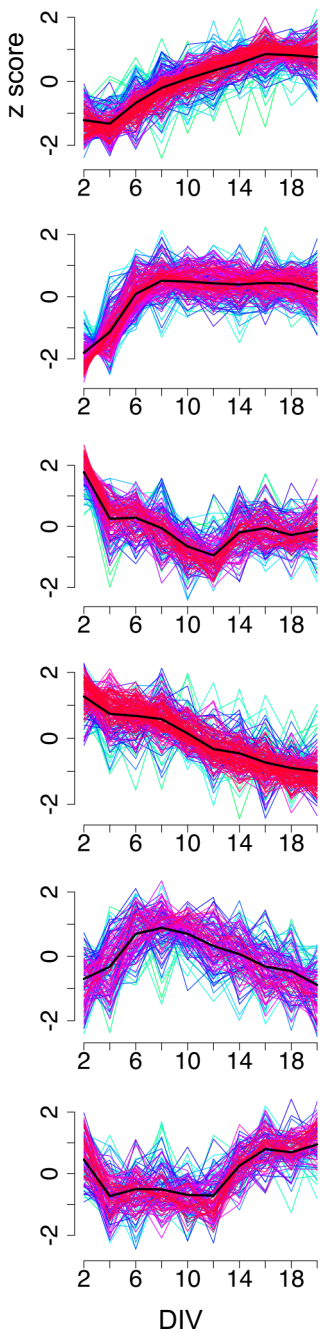


Figure 2

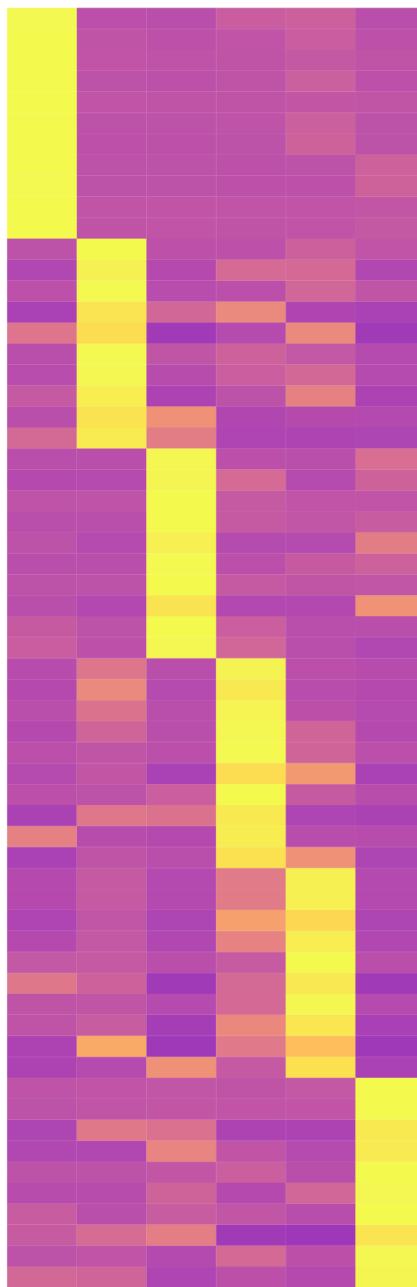
a



b

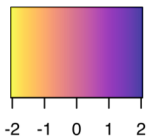
cluster

1 2 3 4 5 6



- CC: postsynapse
- CC: glutamatergic synapse
- CC: presynapse
- CC: axon
- CC: ionotropic glutamate receptor complex
- BP: synaptic signaling
- BP: chemical synaptic transmission
- BP: regulation of membrane potential
- MF: ion channel activity
- MF: neurotransmitter receptor activity
- MF: ligand-gated ion channel activity
- BP: cellular response to tumor necrosis factor
- BP: tissue remodeling
- BP: apoptotic signaling pathway
- BP: cell adhesion mediated by integrin
- BP: synapse assembly
- BP: JAK-STAT cascade
- BP: cytokine production
- BP: regulation of synapse assembly
- BP: drug transmembrane transporter activity
- BP: organic acid transmembrane transporter activity
- CC: endoplasmic reticulum part
- CC: membrane-enclosed lumen
- BP: response to endoplasmic reticulum stress
- BP: macromolecule biosynthetic process
- BP: carbohydrate derivative biosynthetic process
- BP: proteolysis in cellular protein catabolic process
- BP: ERAD pathway
- BP: glycoprotein biosynthetic process
- MF: peptidase inhibitor activity
- MF: enzyme inhibitor activity
- CC: focal adhesion
- CC: cell-substrate adherens junction
- CC: apical plasma membrane
- CC: integrin complex
- BP: cell migration
- BP: cell adhesion
- MF: protein kinase binding
- MF: growth factor binding
- MF: protein heterodimerization activity
- MF: calcium ion binding
- BP: cell projection organization
- BP: plasma membrane bounded cell projection
- BP: generation of neurons
- BP: cell projection morphogenesis
- MF: semaphorin receptor binding
- MF: protein binding
- MF: chemorepellent activity
- MF: binding
- MF: cell adhesion molecule binding
- MF: lipid binding
- CC: vacuolar membrane
- CC: lysosomal membrane
- CC: coated vesicle
- BP: catabolic process
- BP: autophagy
- BP: response to pH
- MF: cofactor binding
- MF: hydrolase activity
- MF: lipid transporter activity
- MF: transition metal ion binding

Color Key



row z-score (log10 adj.p-value)

Membership

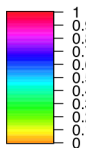


Figure 3

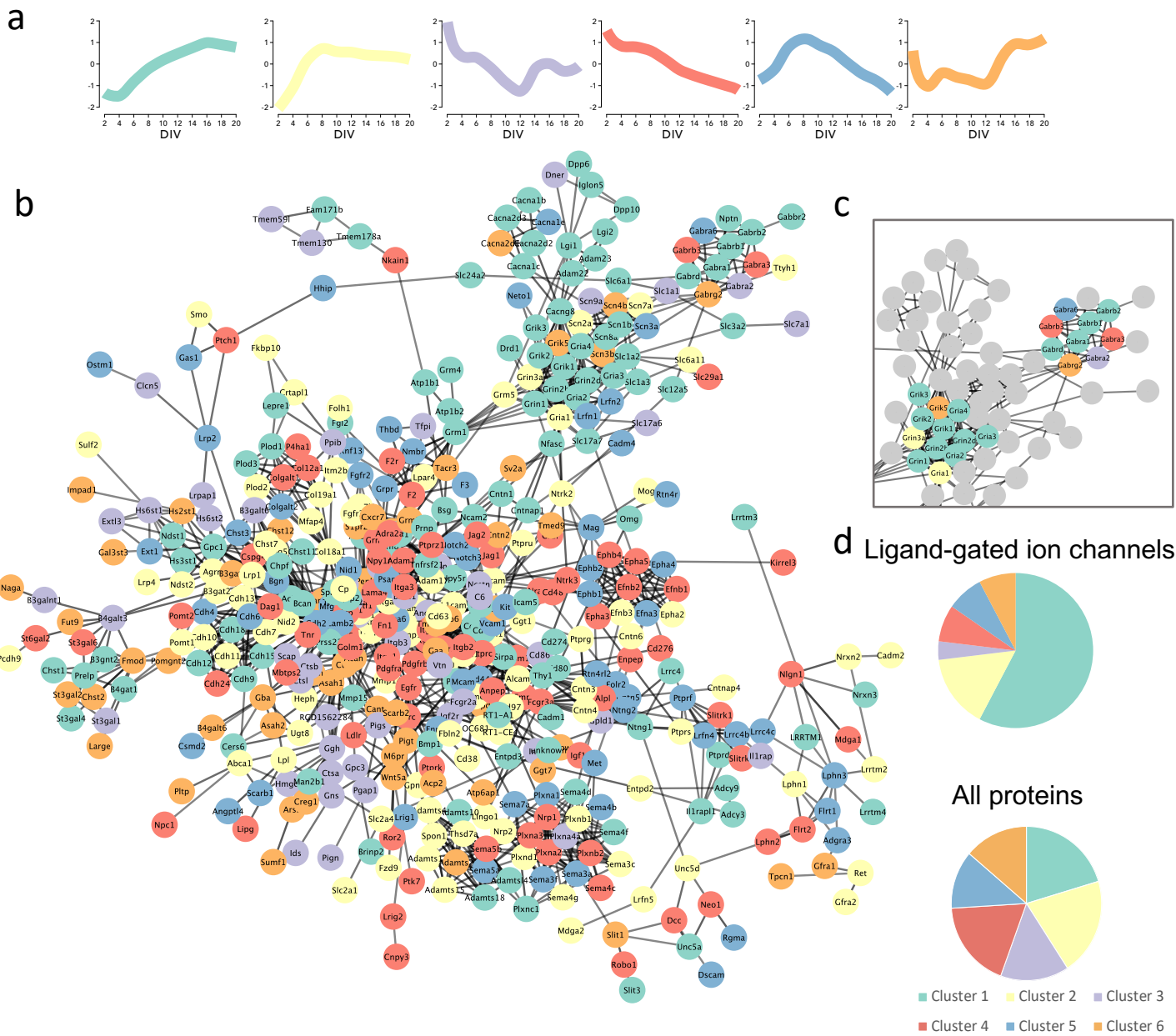


Figure 4

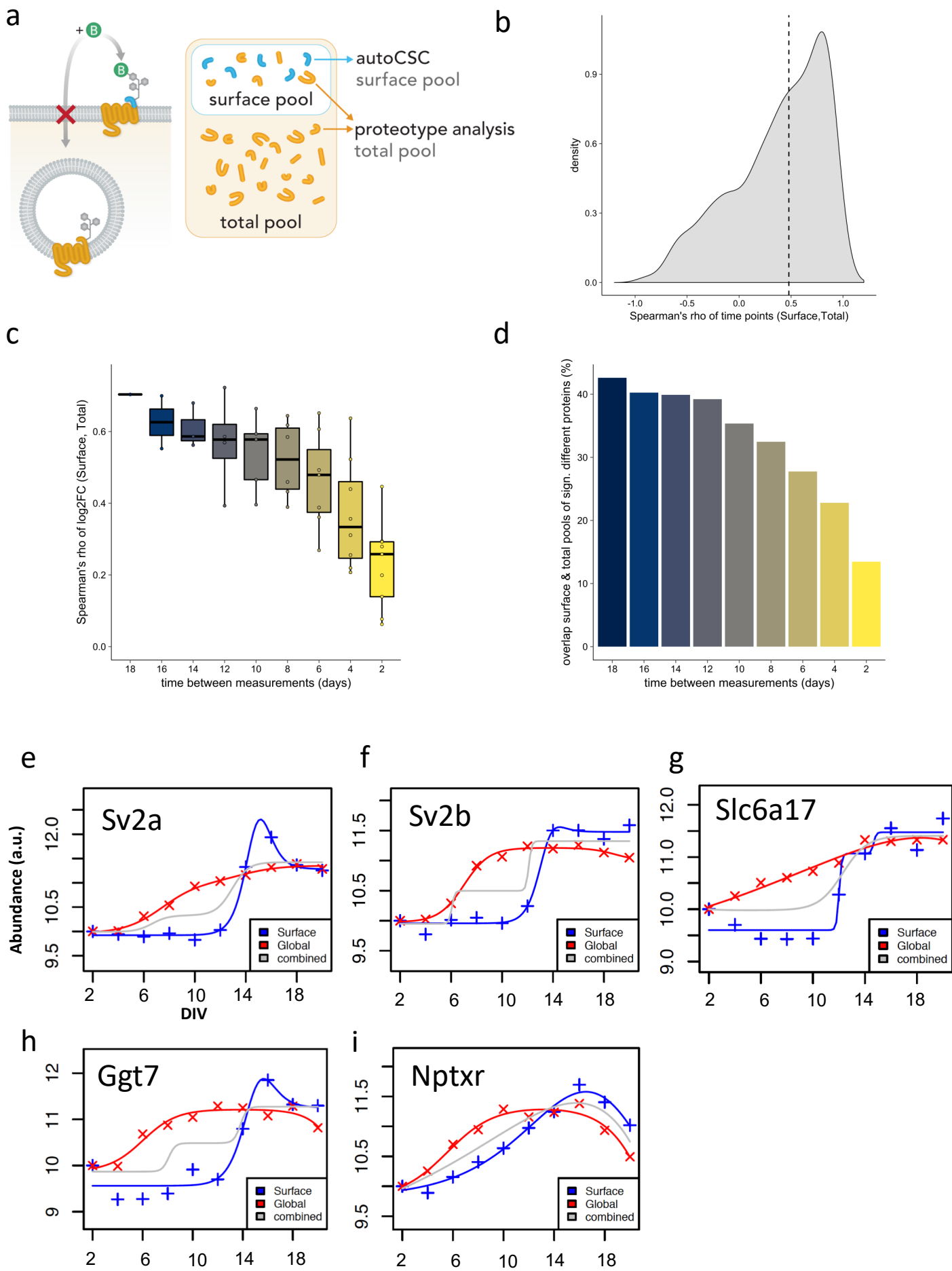


Figure 5

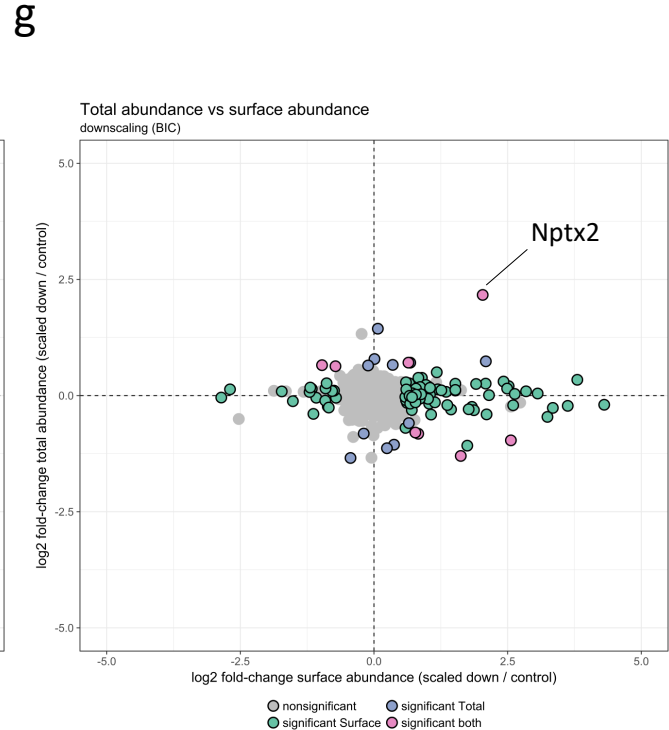
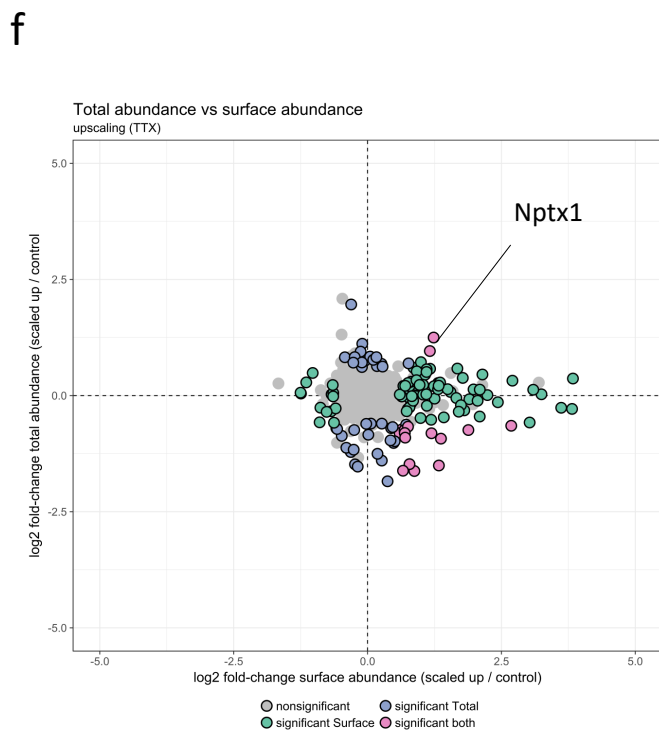
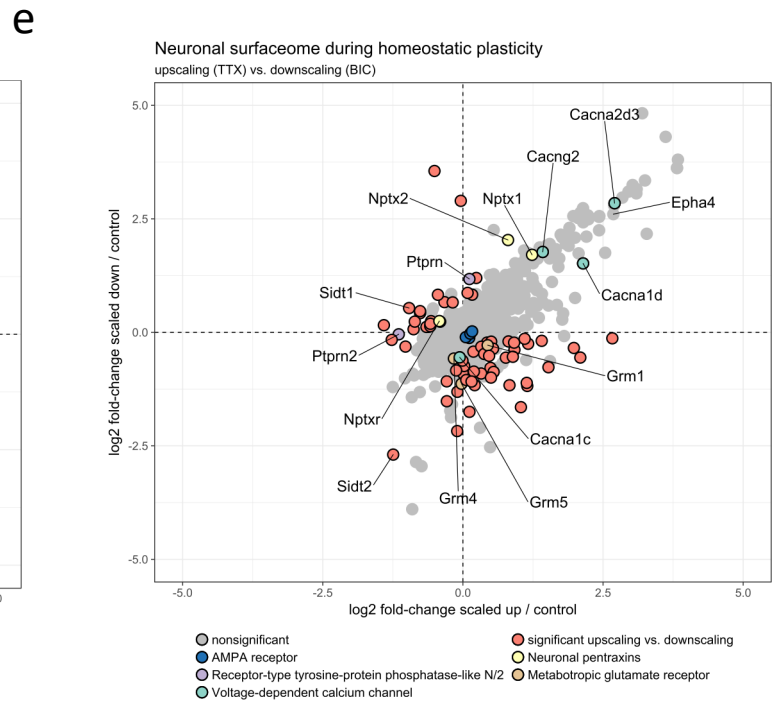
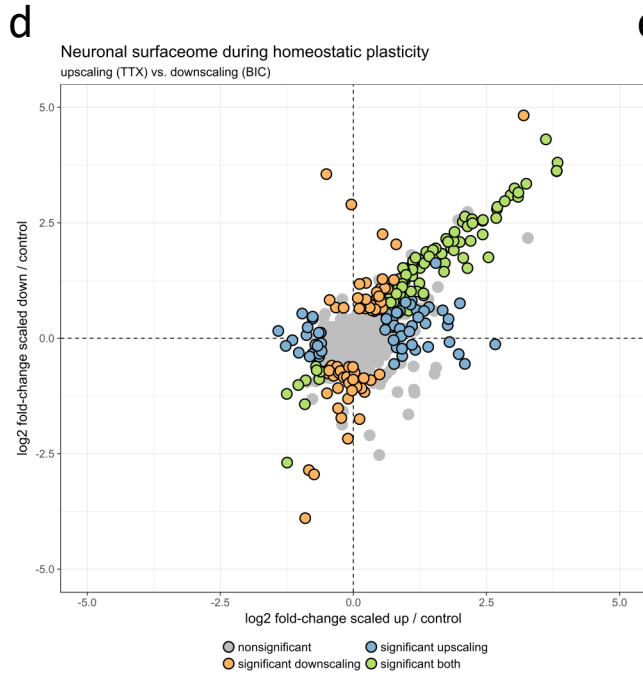
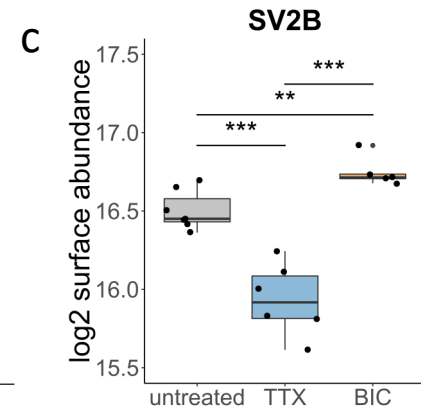
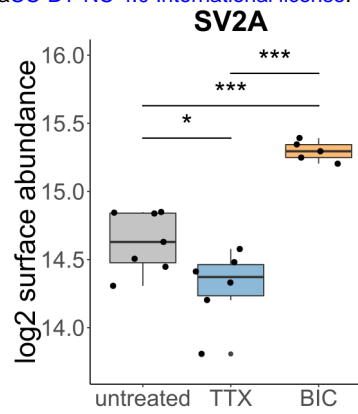
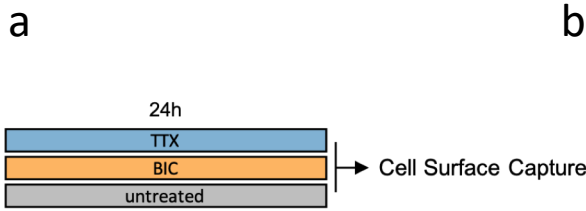


Figure 6

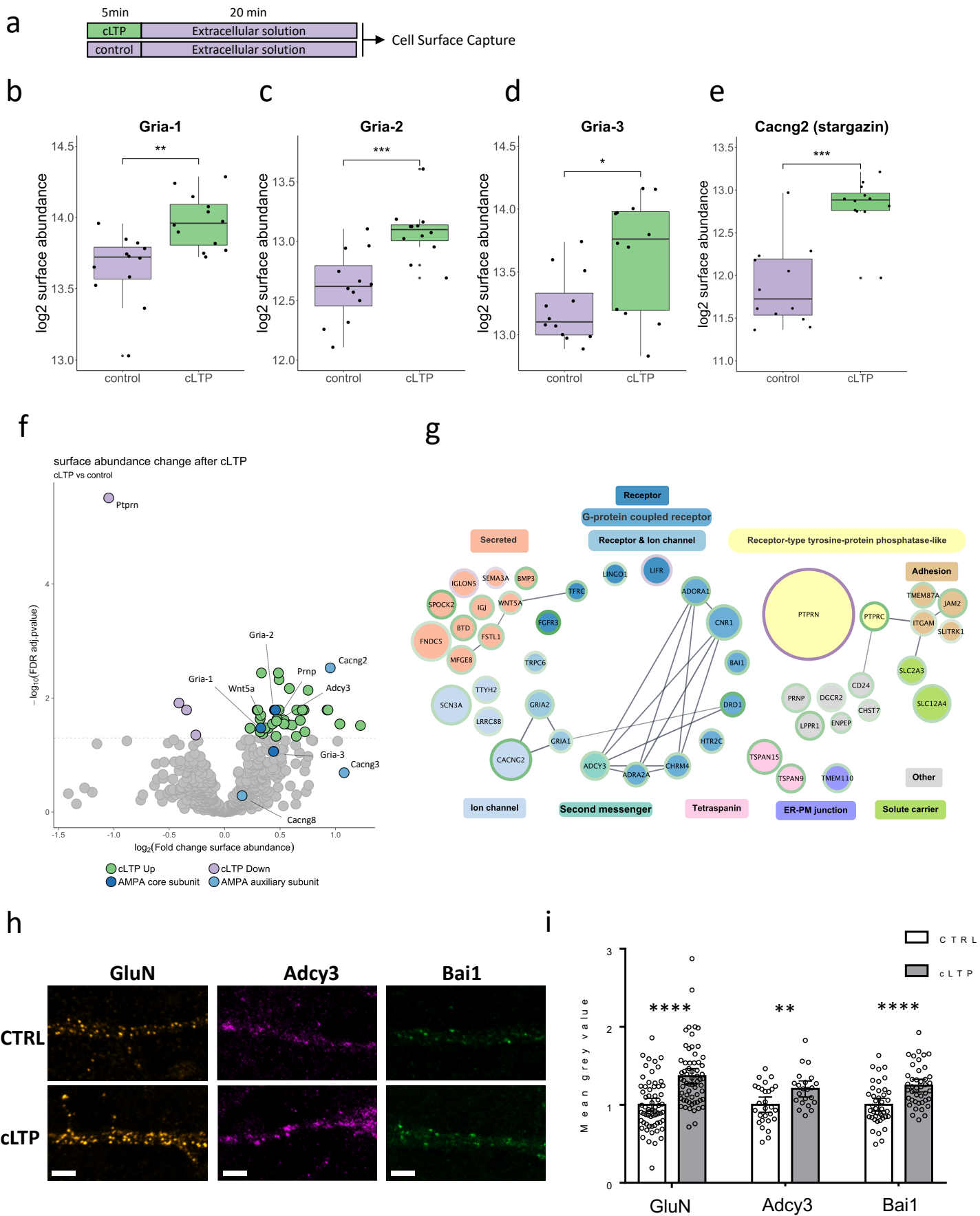


Figure Legends

Figure 1. Quantitative analysis of the neuronal surface during development using autoCSC. **a**, Cultured cortical neurons were collected every second day from 2 DIV to 20 DIV and subjected to autoCSC surface labeling. Live cells were oxidized under mild conditions with sodium-meta-periodate and subsequently labeled with cell-impermeable biocytin-hydrazide. After cell lysis and tryptic digestion, the resulting peptides were subjected to automated processing on a liquid handling robot. Repeated aspiration through filter tips containing streptavidin resin captured biotinylated *N*-glycopeptides. After extensive washing, peptides were released using PNGase F, which catalyzes the cleavage of asparagine-linked glycans. Cleavage leaves a modification (deamidation) at asparagines that can be identified using high-resolution MS. Initially labeled and extracellular peptides are identified by presence of deamidated asparagines within the NXS/T glycosylation consensus sequence, indicating both surface localization and glycosylation site. DIA and targeted feature extraction were used to quantify surface-protein abundances across multiple conditions, providing quantitative surface-abundance profiles across neuronal development in culture. **b**, Qualitative overview of the neuronal surfaceome composition illustrated by intersections of quantified proteins for each time point. **c**, Correlation of all quantified protein abundance values per DIV (median per time point).

Figure 2. Surface abundance profiles reveal developmental stage specific patterns. **a**, unsupervised c-means fuzzy clustering of surface abundance profiles reveals six distinct clusters. Colors indicate cluster membership. **b**, Representative GO annotations for each cluster demonstrating that molecular functions (MF), cellular components (CC), and biological processes (BP) are enriched in at least one cluster ($p < 0.05$, Fisher's exact test).

Figure 3. The neuronal surfaceome interaction network. **a**, Cluster legend showing median cluster profile with the color code used in the string network **b**, String network representation of the largest connected cluster of identified surface proteins; edges represent string confidence of 0.7. **c**, Network representation of ligand-gated ion channels is shown on the top right. **d**, Pie charts of cluster contributions to ligand-gated ion channels and all surfaceome proteins.

Figure 4. Surface abundance does not correlate with total abundance during differentiation. **a**, Comparison of the surface pool against the total protein pool. Peptides analyzed by autoCSC (blue) are surface exposed and thus specifically report on the acute surface pool. Tryptic peptides from the same samples (orange) report the total protein abundance including both intracellular and surface-localized proteins. **b**, Correlation of surface and total abundance protein pools. Spearman's rho of surface and total abundance time series, median indicated with dashed line. **c**, Boxplots of distribution of Spearman's rho for log₂ fold-changes between indicated time intervals for surface and total protein. Boxes indicate median and percentiles (25th and 75th). **d**, Bar chart of counts of overlapping significantly different proteins (fold-change > 1.5 and $p < 0.05$) for comparisons between surface and total pools with respect to interval times. **e-i**, Impulse model fit for data for **e**) Sv2a, **f**) Sv2b, **g**) Slc6a17, **h**) GGt7, and **i**) Nptxr. Crosses indicate normalized median abundance values of three replicates for each time point for surface (blue) and total (red) pools. Lines indicate impulse model fits; grey lines are fits to combined data from surface and total pool analyses .

Figure 5. The neuronal surface is altered during homeostatic plasticity. **a**, Homeostatic plasticity paradigm. **b,c**, Boxplots showing distributions of log₂ surface abundances of **b**) SV2a and **c**) SV2b for replicates of indicated conditions. Boxes indicate median and percentiles (25th and 75th). *p < 0.05, **p < 0.01, ***p < 0.001, t-test. **d**, Scatterplot comparing surface abundance changes during synaptic up- and downscaling. Significantly regulated proteins (fold-change > 1.5 and p < 0.05) are indicated by color. **e**, Scatterplot comparing surface abundance changes during synaptic up- and down-scaling as shown in panel d with protein groups of interest indicated. **f**, Scatterplot showing abundance change (scaling vs. control) of synaptic upscaling comparing surface (x-axis) and total (y-axis) pools. Significantly regulated proteins (fold-change > 1.5 and p < 0.05) are indicated by color. **g**, Scatterplot showing abundance change (scaling vs. control) of synaptic downscaling comparing surface (x-axis) and total (y-axis) pools. Significantly regulated proteins (fold-change > 1.5 and p < 0.05) are indicated by color.

Figure 6. Surface trafficking of diverse cargo during LTP. **a**, chemical LTP paradigm. **b-e**, Boxplots of distributions of log₂ surface abundances for replicates of indicated conditions. Boxes indicate median and percentiles (25th and 75th). **f**, Volcano plot of statistical significance (y-axis) and surface abundance change (x-axis). Horizontal line is located at an adjusted p-value of 0.05. **g**, Proteins with significantly different surface abundances (fold-change > 1.5 and p < 0.05) after cLTP grouped into categories. Shape size indicates scaled -log₁₀ adjusted p-value. Border color indicates fold-change directionality (green > 0, purple < 0). Edges represent string confidence > 0.7. **h**, Representative images of analysed primary dendrites before and after cLTP induction. Bars 5 μm. **i**, Quantification of mean fluorescent intensity of antibody signal on the primary dendrite surface using antibodies against GluN: n=63, Bai1: n=42, Adcy3: n=28 (CTRL) n=22 (cLTP) cells/group. Means + 95% CI presented. ** p<0.01, **** (p<0.0001) using a two-way T-test (Adcy3+Bai1) or Mann-Whitney test (GluN).

Supplementary Figure Legends

Supplementary Figure 1. Quantification of synapse formation in culture. **a**, Representative image of a mature neuronal process used for synapse number quantification. **b**, Relative number of synapses (determined by counting puncta stained with Psd95 and Synapsin or Gephyrin and Synapsin) as a function of time during neurodevelopment in cortical cultures⁸⁵. Boxes indicate median and percentiles (25th and 75th).

Supplementary Figure 2. Overview of unique N-glycosylation sites. Pie chart illustrating overlap of quantified glycosylation sites identified in this study with the UniProt database of quantified proteins. In the Uniprot reference proteome of *Rattus norvegicus*, 73% of proteins are not reviewed and do not contain any annotation on glycosylation sites.

Supplementary Figure 3. Enrichment of GO terms for the neuronal surfaceome. Significantly enriched **a**) cellular components, **b**) molecular functions, and **c**) biological processes for the quantified neuronal surfaceome (p < 0.05, Fisher's exact test) plotted against the protein count for each term.

Supplementary Figure 4. Correlation matrix of all samples and developmental time points. Pearson's correlation of all quantified protein abundance values per DIV for all replicates.

Supplementary Figure 5. Counts of significantly different proteins for neighboring time points. Result of pairwise significance testing for surface and total abundance across the developmental time series. Quantitative values obtained from MSstats.

Supplementary Figure 6. Minimum centroid distance plot for determination of optimal cluster number. Calculation of minimum centroid distance for a range of cluster numbers used to estimate the optimal number of clusters as previously described⁴⁰.

Supplementary Figure 7. Correlation of surface abundance profiles with membership in protein complexes. Density plot of Spearman's correlation coefficients for proteins with a complex member (Corum database, median = 0.55) or all protein combinations (median 0.04) ($p = 1.095e^{-07}$, t-test).

Supplementary Figure 8. Defined protein categories mapped to the neuronal surfaceome string network. **a**, we mapped trans-synaptic cell adhesion molecules⁴⁶ to the surfaceome network. Synaptic cell adhesion molecules as defined in Földy et al.⁴⁶ mapped to the surfaceome network. **b and c**, Proteins encoded by mRNAs enriched in **b**) astrocytes or **c**) neurons⁴⁸ mapped to the largest connected cluster of quantified surface proteins within the string network representation. Edges represent string confidence of 0.7. Pie charts illustrate the proportion of proteins that belong to each cluster.

Supplementary Figure 9. Abundance change for surface and total protein pools for the most distant time points. Left: Scatterplot comparing 2 DIV with 20 DIV. Significantly regulated proteins (fold-change > 1.5 and $p < 0.05$) are indicated by color. Right: Pie chart of protein counts present in quadrants 2 and 4 (18%) and 1 and 3 (82%).

Supplementary Figure 10. Impulse model fit for data from a selection of surface proteins with overlapping surface and total abundance profiles. Crosses indicate normalized median abundance values of three replicates for each time point for surface (blue) and total (red) pools. Lines indicate impulse model fits; grey lines are fits to combined data from surface and total pool analyses⁵⁰.

Supplementary Figure 11. GO terms enriched for modulated surface proteins during homeostatic scaling. Proteins mapping to enriched molecular function (top) and biological processes (bottom) GO terms. Boxes indicate median and percentiles (25th and 75th) ($p < 0.05$, Fisher's exact test).

Supplementary Figure 12. Surface pool responds with higher fold-change differences to synaptic scaling than the total protein pool. Violin plots of distributions of absolute fold-change differences (scaling vs. control) for significantly different proteins (fold-change>1.5 and $p < 0.05$) when surface and total abundances per condition were compared. Circles display underlying data points. Lines in violin represent median and percentiles (25th and 75th). *** $p < 0.001$, t-test.

Supplementary Figure 13. Total proteotype analysis after cLTP. Volcano plot of statistical significance (y-axis) vs. surface abundance change (x-axis). Horizontal line is located at adjusted p-value of 0.05.

Supplementary Figure 14. Adcy3 localizes to synaptic sites. Adcy3 immunoreactivity localises to synaptic sites identified using antibodies reactive for the presynaptic marker synapsin 1/2 (Syn 1/2).

Methods

Chemicals

All chemicals were purchased from Sigma unless stated otherwise.

Primary neuron culture

Dissociated cortical neurons were prepared and maintained as previously described⁸⁶. Briefly, cortices of postnatal day 0-1 rat pups (Sprague-Dawley) were dissociated and plated on poly-L-lysine-coated, 100-mm cell culture dishes (4-5 million cells per dish) or glass coverslips for immunocytochemistry. Cells were maintained in Neurobasal Plus media supplemented with B27 Plus and 2 mM Glutamax (all from Thermo Fisher Scientific) for the indicated number of days. Cytosine-D-arabino-furanoside (araC; 5 μ M) was added to the medium on 4 DIV to prevent overgrowth of astrocytes. For microscopy LTP validation experiments, cortical cultures were prepared from E17 rat embryos as previously described⁸⁷. For cLTP for autoCSC, the cell culture medium was removed, and cells were placed either in extracellular solution (120 mM NaCl, 3 mM KCl, 10 mM D-glucose, 10 mM HEPES, B27 Plus, 2 mM Glutamax, MEM amino acids, 2 mM MgSO₄, 2 mM CaCl₂, pH 7.4) or cLTP buffer (same as extracellular solution but with 0 mM MgSO₄, 3 mM CaCl₂, 30 μ M bicuculline, 200 μ M glycine) for 5 min, followed by 20 min in extracellular solution before autoCSC surface labeling.

All experiments were carried out with the approval of the local animal experiment authorities.

Cell surface capture - labeling and digestion

Surface glycoproteins on live cells were gently oxidized with 2 mM NaIO₄ (20 min, 4 °C) in labeling Buffer (LB) consisting of PBS, pH 6. Cells were washed once in LB and subsequently biotinylated in LB containing 5 mM biocytin hydrazide (Pitsch Nucleic Acids) and 5 mM 5-methoxyanthranilic acid for 1 h at 4 °C min. Experiments with homeostatic scaling and cLTP were performed using 2-(aminomethyl)benzimidazole (50 mM)⁸⁸ instead of 5-methoxyanthranilic acid as catalyst. Cells were washed three times with LB and harvested, lysed in lysis buffer (100 mM Tris, 1% sodium deoxycholate, 10 mM TCEP, 15 mM 2-chloroacetamide) by repeated sonication using a VialTweeter (Hielscher Ultrasonics), and heated to 95 °C for 5 min. Proteins were digested with LysC (Wako Chemicals) and trypsin overnight at 37 °C using an enzyme-to-protein ratio of 1:200. In order to inactivate trypsin and precipitate deoxycholate, samples were boiled for 20 min, acidified with 10% formic acid to approximately pH 3, and centrifuged 10 min at 16,000 g. Peptide concentrations were determined in the supernatant using a NanoDrop 2000 instrument (Thermo Fisher Scientific) and normalized before aliquoting into a 96-well sample plate for automated processing. For total proteotype analysis, a fraction of the digested proteins was separated and desalted for liquid chromatography–tandem mass spectrometry (LC-MS/MS) analysis as described below.

Automated processing

A Versette liquid handling robot (Thermo Fisher Scientific) equipped with a Peltier element was used to adjust the temperature within 96-well plates during glycopeptide elution. Streptavidin tips were prepared by pushing a bottom filter membrane into disposable automation tips (Thermo Fisher Scientific). Each tip was filled with 80 μ l of Pierce Streptavidin Plus UltraLink Resin (Thermo Fisher Scientific), and tips were sealed by compressing the resin with a top filter

membrane. Assembled tips were attached to the liquid handling robot and washed with 50 mM ammonium bicarbonate by repeated cycles of aspiration and dispensing (mixing). Biotinylated peptides were bound to the streptavidin resin over 2.5 h of mixing cycles. Subsequently the streptavidin tips were sequentially washed with 5 M NaCl, StimLys Buffer (100 mM NaCl, 100 mM glycerol, 50 mM Tris, 1% Triton X-100), with 50 mM ammonium bicarbonate, 100 mM NaHCO₃ (pH 11), and with 50 mM ammonium bicarbonate. For glycopeptide elution, streptavidin tips were incubated overnight in 50 mM ammonium bicarbonate containing 1,000 units PNGase F (New England Biolabs) at 37 °C. The sample plate was then removed from the liquid handling robot and acidified to pH 2–3 with formic acid. Peptides were desalted with C18 UltraMicroSpin columns (The Nest Group) according to the manufacturer's instructions and dried in a SpeedVac concentrator (Thermo Fisher Scientific).

Liquid chromatography–tandem mass spectrometry analysis

For MS analysis, peptides were reconstituted in 5% acetonitrile and 0.1% formic acid containing iRT peptides (Biognosys) and analyzed in DIA and DDA modes for spectral library generation. For spectral library generation, a fraction of the samples originating from the same condition were pooled to generate mixed pools for each condition. Peptides resulting from autoCSC were separated by reverse-phase chromatography on a high-pressure liquid chromatography (HPLC) column (75- μ m inner diameter; New Objective) packed in-house with a 15-cm stationary phase ReproSil-Pur 120A C18 1.9 μ m (Dr. Maisch GmbH) and connected to an EASY-nLC 1000 instrument equipped with an autosampler (Thermo Fisher Scientific). The HPLC was coupled to a Q Exactive plus mass spectrometer equipped with a nanoelectrospray ion source (Thermo Fisher Scientific). Peptides were loaded onto the column with 100% buffer A (99% H₂O, 0.1% formic acid) and eluted at a constant flow rate of 300 nL/min with increasing buffer B (99.9% acetonitrile, 0.1% formic acid) over a nonlinear gradient. The DIA method (Bruderer et al. 2015) contained 14 DIA segments of 35,000 resolution with IT set to auto, AGC of 3×10^6 , and a survey scan of 70,000 resolution with 120 ms max IT and AGC of 3×10^6 . The mass range was set to 350–1650 m/z. The default charge state was set to 2. Loop count 1 and normalized collision energy stepped at 25.5, 27.5, and 30. For the DDA, a TOP12 method was recorded with 60,000 resolution of the MS1 scan and 20 ms max IT and AGC of 3×10^6 . The MS2 scan was recorded with 70,000 resolution of the MS1 scan and 120 ms max IT and AGC of 3×10^6 . The covered mass range was identical to the DIA.

For total proteotype analysis, peptides were separated by reverse-phase chromatography on an HPLC column (75- μ m inner diameter; New Objective) packed in-house with a 50-cm stationary phase ReproSil-Pur 120A C18 1.9 μ m (Dr. Maisch GmbH) and connected to an EASY-nLC 1000 instrument equipped with an autosampler (Thermo Fisher Scientific). The HPLC was coupled to a Fusion mass spectrometer equipped with a nanoelectrospray ion source (Thermo Fisher Scientific). Peptides were loaded onto the column with 100% buffer A (99% H₂O, 0.1% formic acid) and eluted with increasing buffer B (99.9% acetonitrile, 0.1% formic acid) over a nonlinear gradient for 240 min. The DIA method³⁹ contained 26 DIA segments of 30,000 resolution with IT set to 60 ms, AGC of 3×10^6 , and a survey scan of 120,000 resolution with 60 ms max IT and AGC of 3×10^6 . The mass range was set to 350–1650 m/z. The default charge state was set to 2. Loop count 1 and normalized collision energy was stepped at 27. For the DDA, a 3-s cycle time method was recorded with 120,000 resolution of the MS1 scan and 20 ms max IT and AGC of 1×10^6 . The

MS2 scan was recorded with 15,000 resolution of the MS1 scan and 120 ms max IT and AGC of 5×10^4 . The covered mass range was identical to the DIA. The mass spectrometry proteomics data have been deposited to the ProteomeXchange Consortium via the PRIDE⁸⁹ partner repository with the dataset identifier PXD014790 (user: reviewer14671@ebi.ac.uk, password: rNIMlesc).

High-pH fractionation of peptides

High-pH fractionation was performed as previously described⁹⁰. Briefly, samples were resuspended in Buffer A (20 mM ammonium formate and 0.1% ammonia solution in water, pH 10) and 200 µg of sample was injected into an Agilent Infinity 1260 (HP Degasser, Vial Sampler, Cap Pump) and 1290 (Thermostat, FC-µS) system. The peptides were separated at 30 °C on a YMC-Triart C18 reversed-phase column with a diameter of 0.5 mm, length of 250 mm, particle size of 3 µm, and pore size of 12 nm. At a flow of 11 µL/min, the peptides were separated by a linear 56-min gradient from 5% to 35% Buffer B (20 mM ammonium formate, 0.1% ammonia solution, 90% acetonitrile in water, pH 10) against Buffer A (20 mM ammonium formate, 0.1% ammonia solution, pH 10) followed by a linear 4-min gradient from 35% to 90% Buffer B against Buffer A and 6 min at 90% Buffer B. The resulting 36 fractions were pooled into 12 samples. The buffer of the pooled samples was evaporated using vacuum centrifugation at 45 °C.

Data analysis of DIA LC-MS/MS

LC-MS/MS DIA runs were analyzed with Spectronaut Pulsar X version 12 (Biognosys)^{38,39} using default settings. Briefly, a spectral library was generated from pooled samples measured in DDA as described above. The collected DDA spectra were searched against UniprotKB (UniProt reference proteome including isoforms for *Rattus norvegicus*, retrieved September 2018) using the Sequest HT search engine within Thermo Proteome Discoverer version 2.1 (Thermo Fisher Scientific). We allowed up to two missed cleavages and semi-specific tryptic digestion. Carbamidomethylation was set as a fixed modification for cysteine, oxidation of methionine and deamidation of arginine were set as variable modifications. Monoisotopic peptide tolerance was set to 10 ppm, and fragment mass tolerance was set to 0.02 Da. The identified proteins were assessed using Percolator and filtered using the high peptide confidence setting in Protein Discoverer. Analysis results were then imported to Spectronaut Pulsar version 12 (Biognosys) for the generation of spectral libraries.

Targeted data extraction of DIA-MS acquisitions was performed with Spectronaut version 12 (Biognosys AG) with default settings as previously described^{38,39}. The proteotypicity filter “only protein group specific” was applied. Extracted features were exported from Spectronaut using “Quantification Data Filtering” for statistical analysis with MSstats (version 3.8.6)⁹¹ using default settings. Briefly, features were filtered for use for calculation of Protein Group Quantity as defined in Spectronaut settings, common contaminants were excluded. For autoCSC, the presence of consensus NXS/T sequence including a deamidation (+0.98 Da) at asparagine was required. For each protein, features were log-transformed and fitted to a mixed effect linear regression model for each sample in MSstats⁹¹. In MSstats, the model estimated fold change and statistical significance for all compared conditions. Significantly different proteins were determined by the threshold fold-change > 1.5 and adjusted p-value < 0.05. Benjamini-Hochberg method was used to account for multiple testing. In the comparison of all developmental time points with each other, p-value adjustment was performed on surface proteins with a fold-change > 1.5. Protein

abundance per sample or condition was used for further analysis and plotting. The neurodevelopmental time series autoCSC experiment was performed with three biological replicates for 10 time points, one sample from 4 DIV was excluded due to technical error, generating 29 samples for final quantification for autoCSC. Homeostatic scaling autoCSC experiment was performed with seven biological replicates per condition, outliers were removed to generate 18 samples for final quantification. The cLTP autoCSC experiment was performed with twelve biological replicates per condition generating 24 samples for final quantification.

Glycosylation site analysis

For glycosylation site counting the following rules were followed: i) only glycosylated peptides conforming to the NX[STC] consensus sequence were considered; ii) to avoid inflating the count, non-proteotypic peptides were arbitrarily assigned to a single protein in the protein group; iii) if a glycosylated peptide could be mapped to multiple positions within the same protein, both positions were kept, unless one of the mappings resulted in a higher number of sites matching the consensus NX[STC] motif, in which case only this one was kept. When comparing the glycosylation sites identified in this study to the ones annotated in UniProt, only proteins identified in this study as having at least one glycosylation site were considered in UniProt.

Data analysis - correlation, clustering, impulse model

All further analysis was done based on quantitative values obtained from MSstats. Upset plots were generated using the group quantification table in UpsetR⁹². GO analysis of the neuronal surfaceome composition was performed with EnrichR⁹³. Correlation analysis and significance testing was performed in MSstats were calculated in R using standard functions. For fuzzy c-means clustering of surface abundance profiles we used mfuzz⁴⁰, and topGO was used for GO annotation of resulting clusters⁹⁴. For comparison of surface and total abundance pools, quantitative values from MSstats were merged by protein groups. Protein groups were considered matching if at least one Uniprot protein entry of the surface protein group was found in a protein group from the total proteotype analysis. Impulse modeling and significance testing were performed with ImpulseDE⁵⁰ using default settings for two time courses. As input, we used quantitative values for each condition (surface and total) from MSstats. Prior to ImpulseDE, both surface and total time series were centered around 2 DIV by subtracting the value of 2 DIV from each time point and 10 was added to each data point to avoid negative values.

Immunocytochemistry – synapse counts

Cells were washed in PBS and fixed in 4% PFA for 15 min at room temperature. After washing in PBS, cells were permeabilized with 0.25% Triton X-100 in PBS for 5 min and blocked with PBS containing 10% BSA for 30 min at 37 °C. Cultures were stained with primary antibodies against PSD95 (mouse monoclonal, clone 6G6-1C9, Thermo Fisher Scientific, 1:1000) and gephyrin (recombinant rabbit purified IgG, clone RbmAb7a, Synaptic Systems, 1:500) in PBS containing 5% BSA overnight at room temperature. After washing, cells were incubated with secondary antibodies (anti-mouse IgG Alexa Fluor 555, Molecular Probes A21424, 1:500 and donkey anti-rabbit IgG H&L Alexa Fluor 647, Abcam ab150075, 1:500) for 45 min at room temperature. After washing in PBS, cells were incubated with primary antibody against synapsin (monoclonal mouse IgG fluorescently labeled with Oyster 488, clone 46.1, Synaptic Systems, 1:1000) in PBS

containing 5% BSA for 4 h. Cells were washed again in PBS and mounted on slides in Prolong Gold Antifade (Thermo Fisher Scientific). Images were acquired using a 63x 1.4NA Oil Plan-Apochromat DIC M27 objective on a Zeiss LSM 880 upright laser scanning confocal microscope. Z-stacks of 10 random positions on 3-4 different coverslips were taken per DIV. Maximum intensity projections were analyzed using Synapse Counter plugin for ImageJ with default settings⁸⁵.

Immunocytochemistry - LTP validation

cLTP was performed on DIV 14 neuron cultures plated on glass coverslips via coverslip transfer from home media to either blocking solution (control; 117 mM NaCl, 5.3mM KCl, 30 mM D-glucose, 26mM NaH₂CO₃, 1mM NaH₂PO₄, 15 mM HEPES, B27, 2 mM Glutamax, MEM amino acids, 2 mM MgSO₄, 2 mM CaCl₂) or cLTP solution (same as control but with 0 mM MgSO₄, 3 mM CaCl₂, 30 µM bicuculline, 200 µM glycine) for 5 minutes, followed by 20 minutes recovery in blocking solution before live immuno-staining. Antibodies targeting the extracellular domains of ADGRB1 (ABR-021, Alomone), AMPARs (182 411, Synaptic Systems), and AC3 (AAR-043, Alomone) were diluted 1:100 in blocking solution containing 10% normal goat serum (NGS) and incubated with the cells for 60 minutes. Cells were washed 3x in PBS before live staining at 4°C for 60 min, then washed 3x in PBS before fixation in 4% PFA. Cells were permeabilized with 0.1% Triton in PBS with 10% NGS prior to intracellular labelling of synapsin (106 004, Synaptic Systems) at 1:1000 for 90 minutes at room temperature. Cells were washed 3x in PBS before labelling with secondary antibodies conjugated to Alexa 647, Alexa 488, or Cy3 (Jackson Immuno Research) for 30 min at room temperature, then washed 3x with PBS. Imaging was performed using a LSM800 confocal microscope (Zeiss) with a 40X objective (NA 1.4) at 16 bit depth under non-saturating conditions using a step size of 0.5 µm for a total of 6 z-stacks. Image analysis was performed on the proximal section of principal dendrites (each sample represents one neuron). For total intensity measurements ImageJ was used to quantify the summed intensity across all z-stacks. For synaptic puncta analysis, a custom in house ImageJ macro described previously⁸⁷ was used to quantify the number of puncta per unit area (density) as well as puncta size and integrated density. Mean differences between control and cLTP conditions were analysed using either a two-way t-test (for normally distributed data) or a Mann-Whitney test (for non-normally distributed data) using Prism 5 (GraphPad).

Author contributions

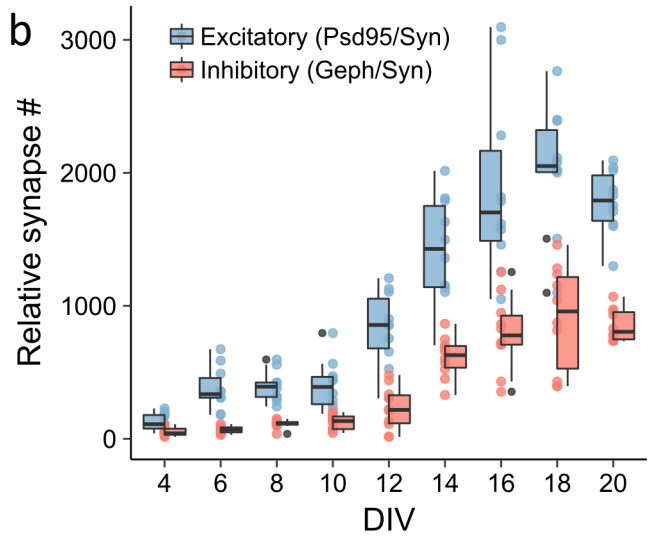
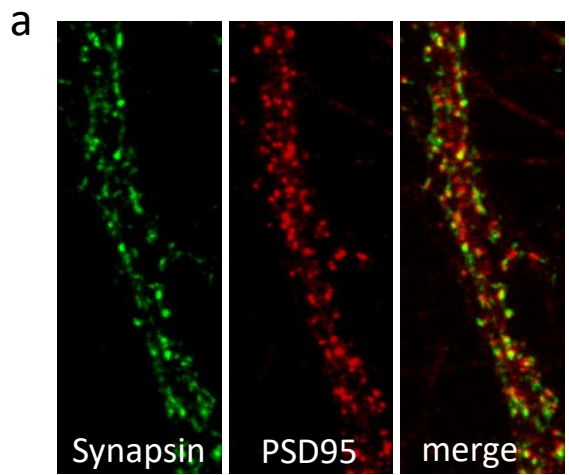
M.v.O. designed, conducted, and analyzed experiments and wrote the manuscript. M.M. contributed new analytical tools. P.G.A.P. performed glycosylation site analysis. B.C. and S.K.T. performed immunocytochemistry LTP validation experiments. B.W. supervised the project and wrote the manuscript. All authors edited the manuscript.

Acknowledgements

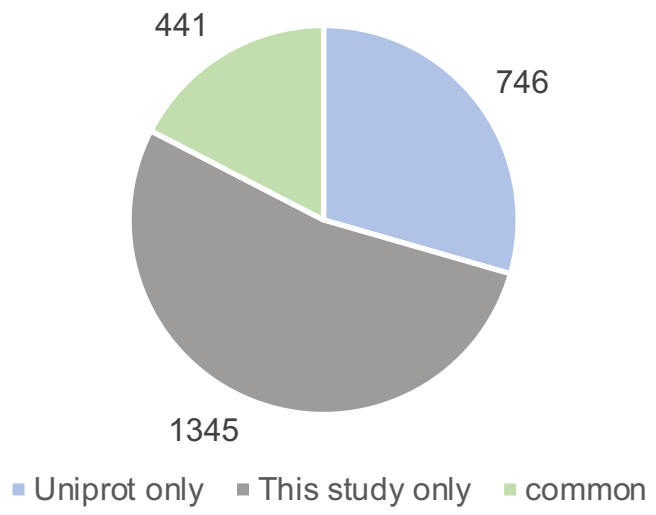
We are grateful to the members of the Wollscheid and Aebersold research groups for discussion and support at all stages of the project. We thank M. Stamou for teaching and sharing experimental procedures; J. R. Wyatt for editing; T. Spletstoeser for graphical support; R. Aebersold, I. Mansuy and E. Schuman for discussions and sharing of experimental procedures; M. Kopf, J. Kieselow, A. Alitalo and EPIC staff for support with animal experimentation; and T.

Schwarz and ScopeM for support with microscopy. For funding, we acknowledge the ETH (grant ETH-30 17-1 and grant ETH-25 15-2) and the Novartis Foundation for Biomedical Research and the Swiss National Science Foundation (grant 31003A_160259 for B.W).

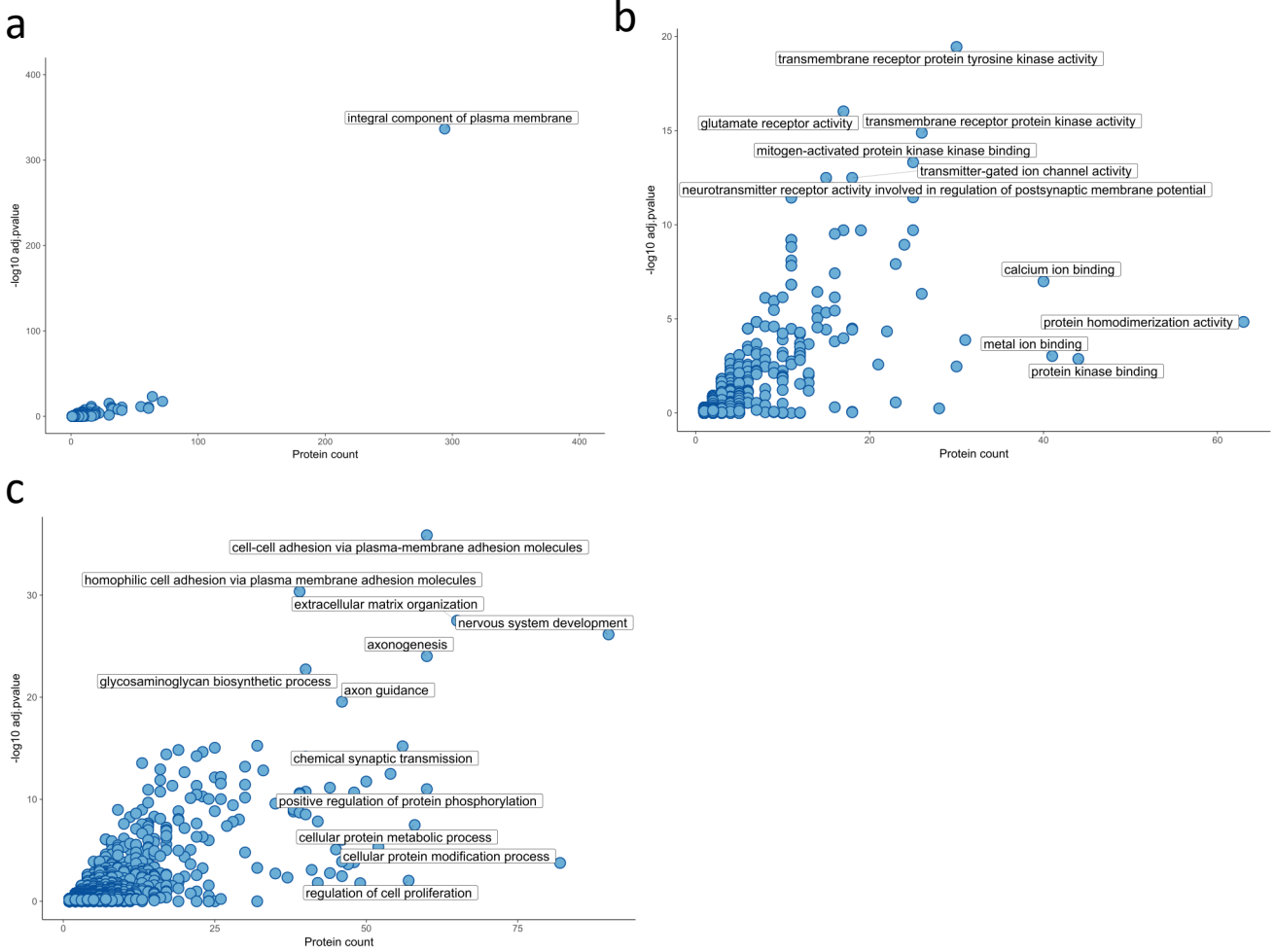
Supplementary Figure 1



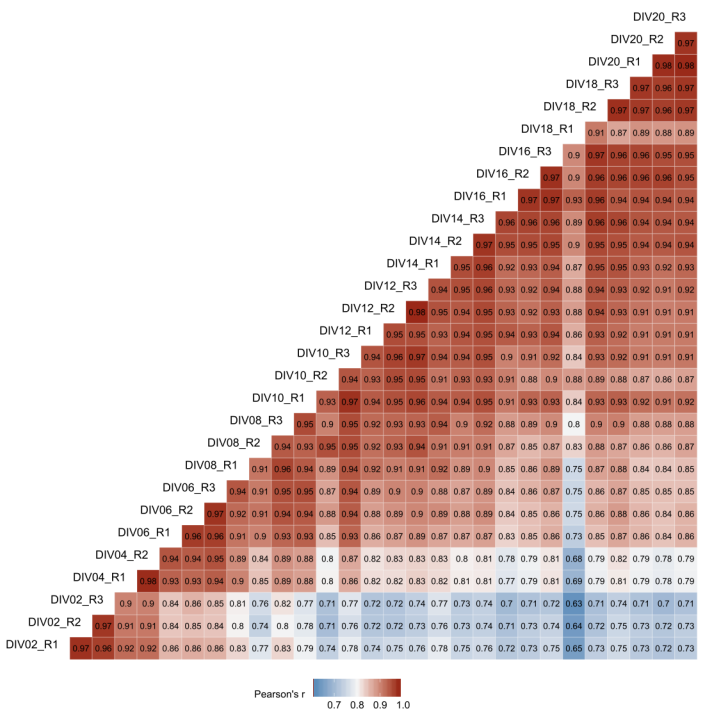
Supplementary Figure 2



Supplementary Figure 3



Supplementary Figure 4

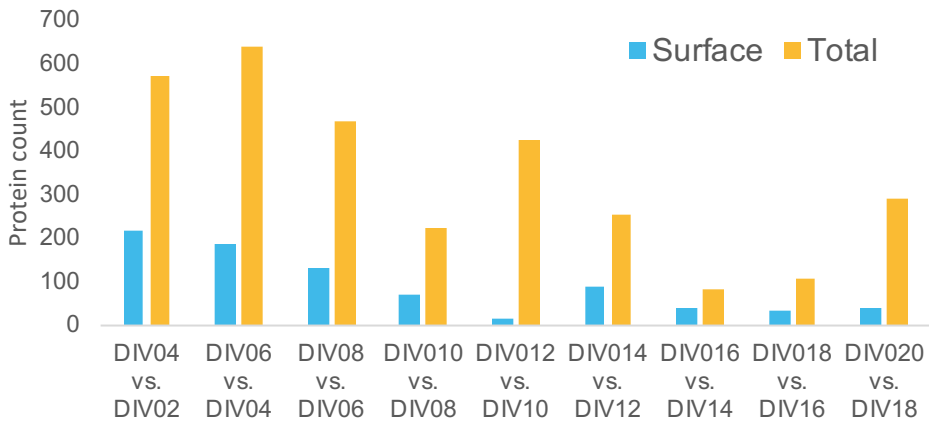


Pearson's r 0.7 0.8 0.9 1.0

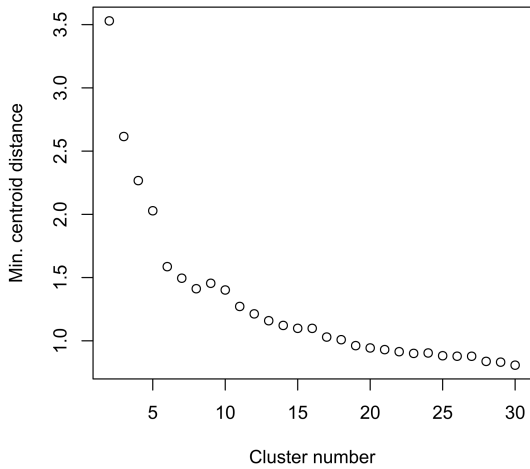
Supplementary Figure 5

Significantly different proteins

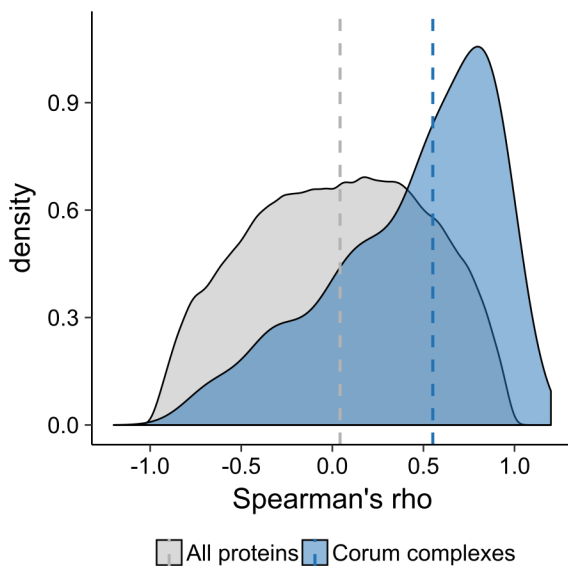
(fold-change > 1.5 | and adj. p-value < 0.05)



Supplementary Figure 6

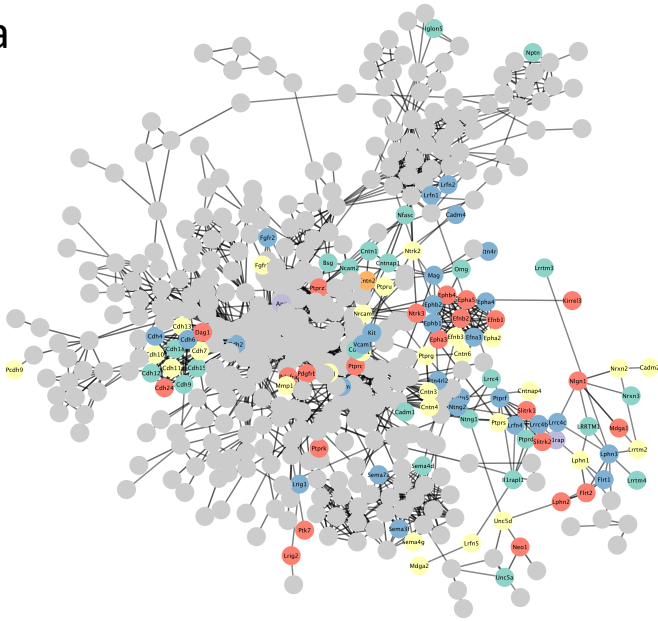


Supplementary Figure 7

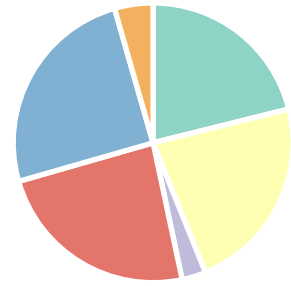


Supplementary Figure 8

a

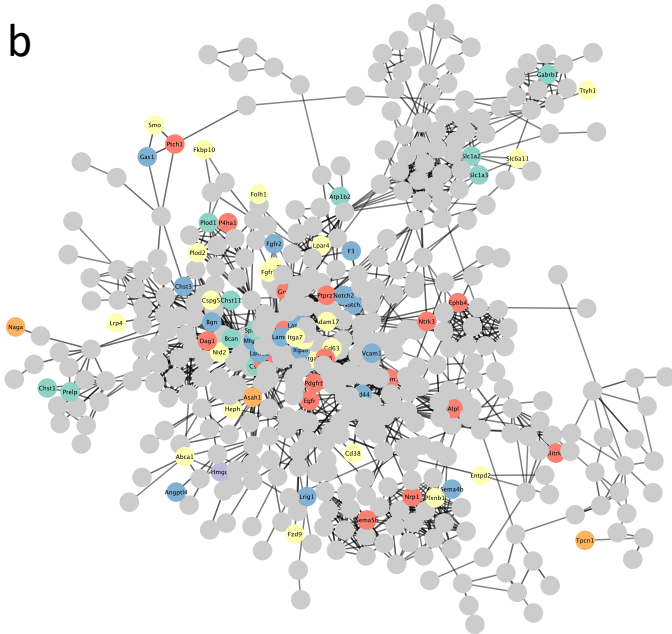


Cell Adhesion Molecules

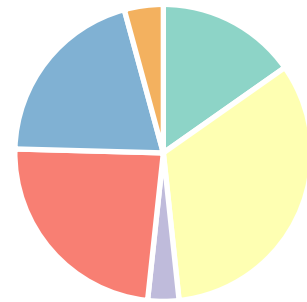


Cluster 1
Cluster 2
Cluster 3
Cluster 4
Cluster 5
Cluster 6

b

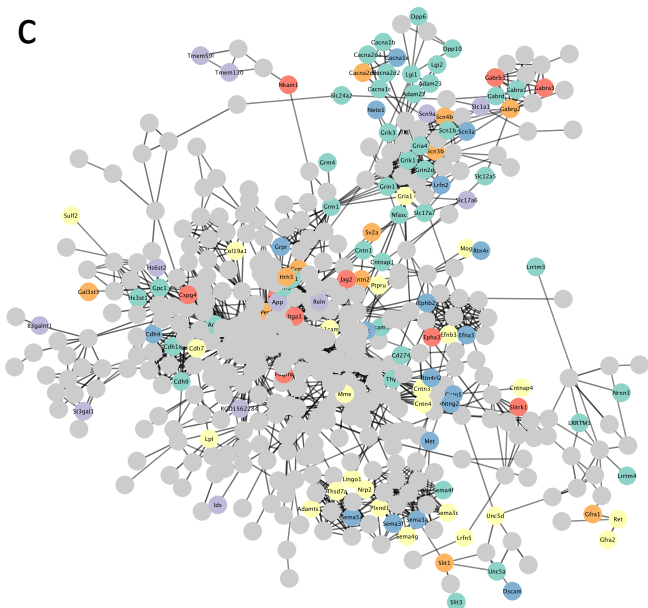


Astrocyte-enriched mRNA

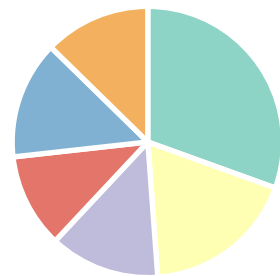


Cluster 1
Cluster 2
Cluster 3
Cluster 4
Cluster 5
Cluster 6

c

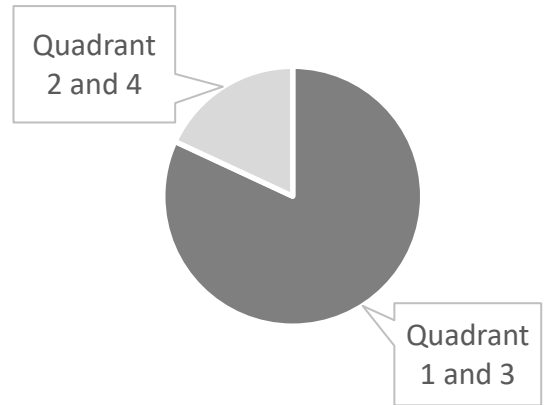
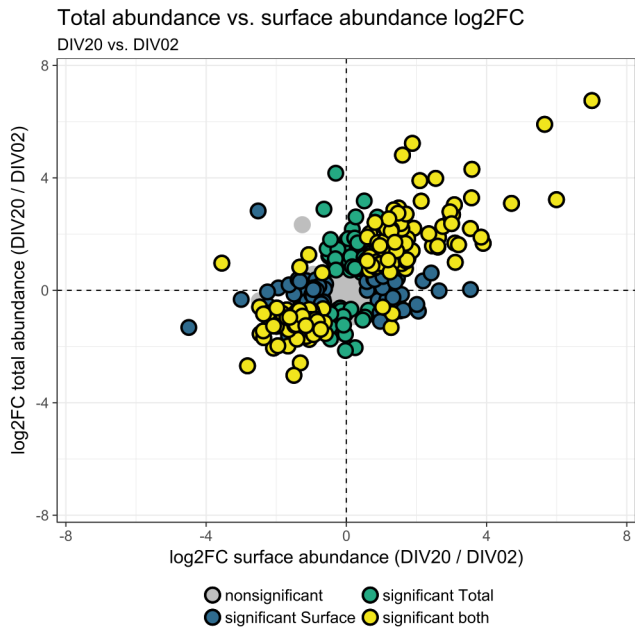


Neuron-enriched mRNA

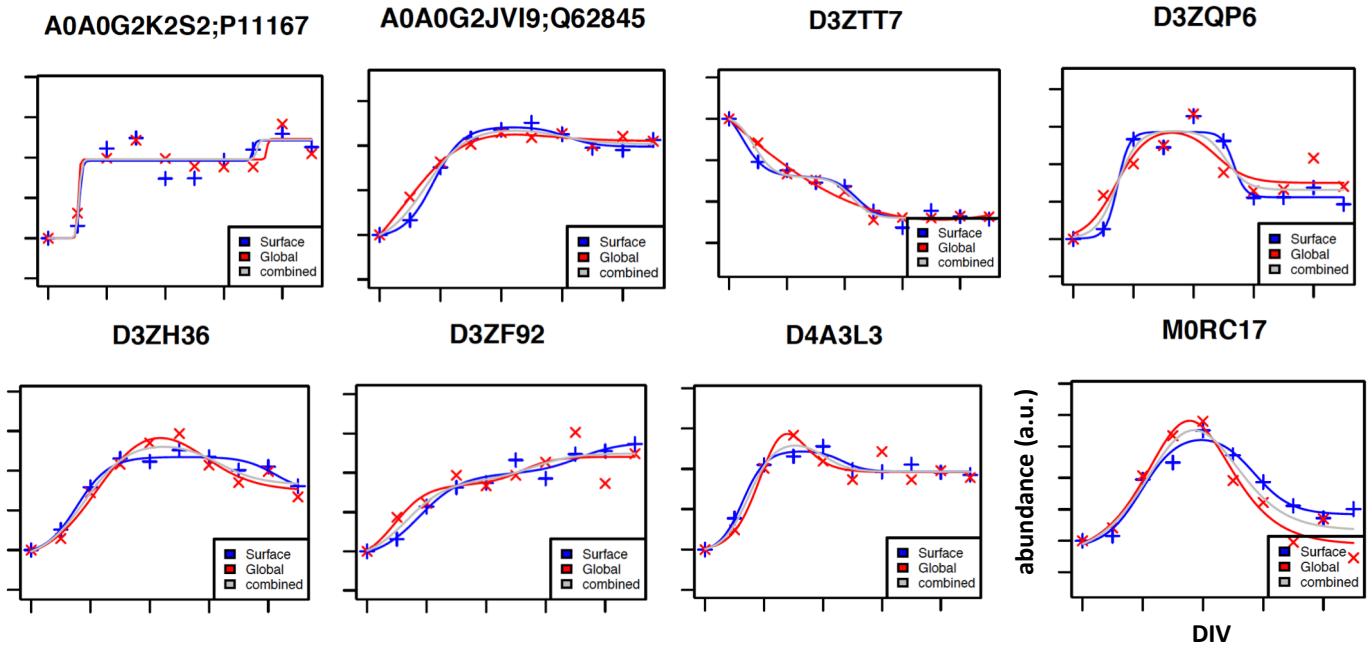


Cluster 1
Cluster 2
Cluster 3
Cluster 4
Cluster 5
Cluster 6

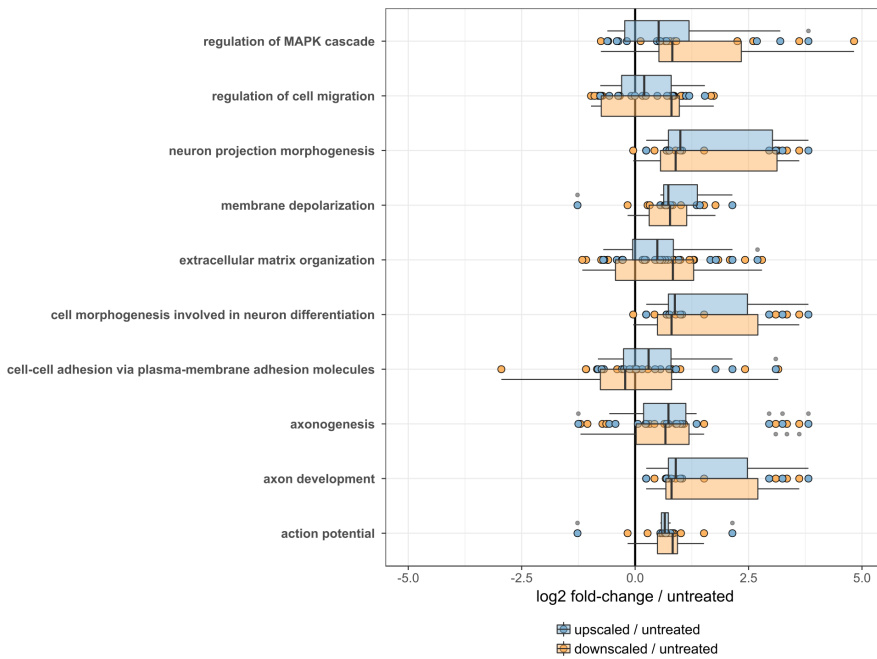
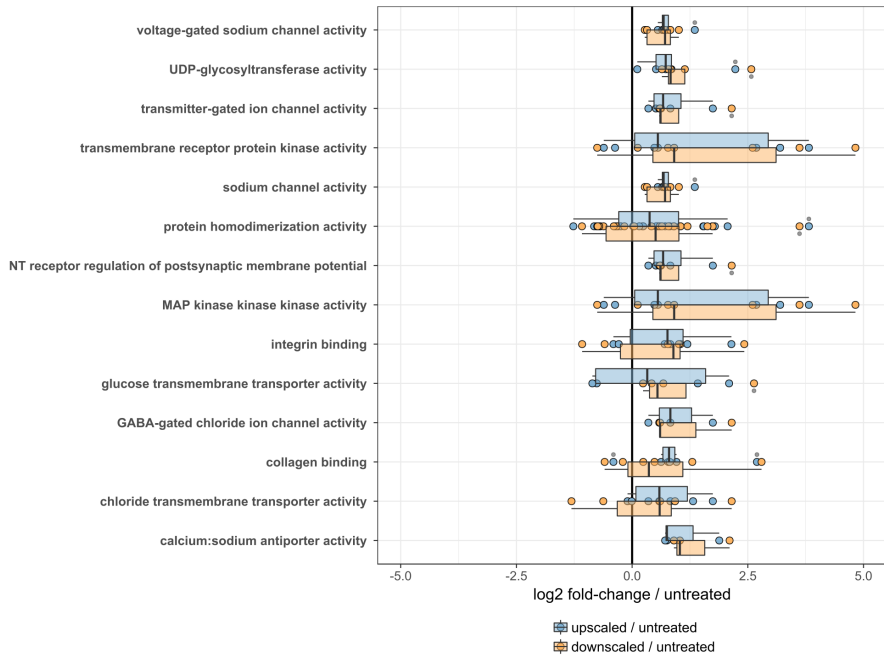
Supplementary Figure 9



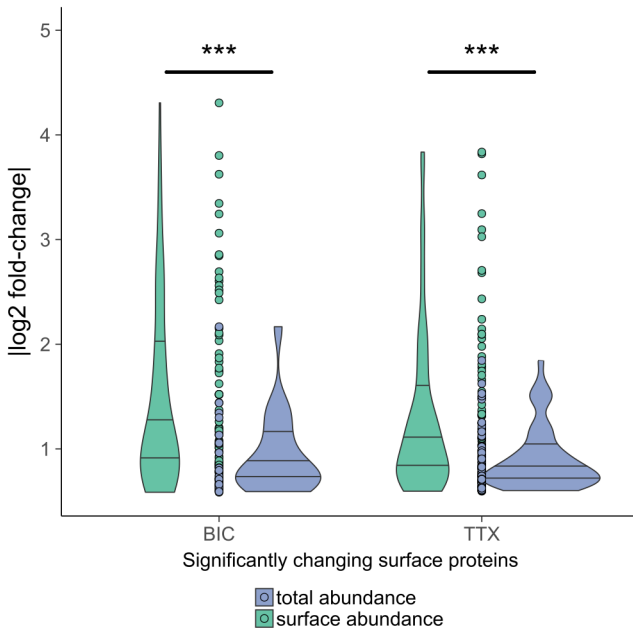
Supplementary Figure 10



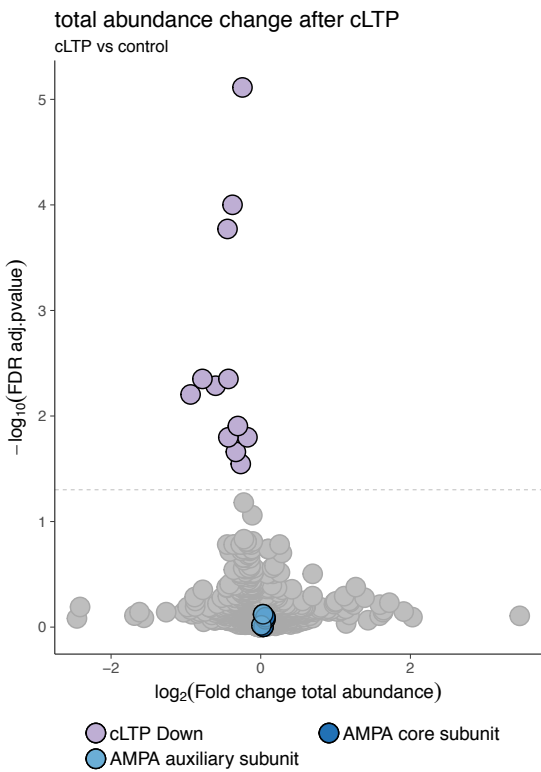
Supplementary Figure 11



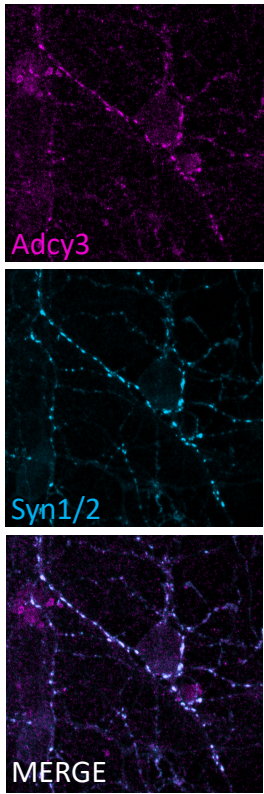
Supplementary Figure 12



Supplementary Figure 13



Supplementary Figure 14



References

- 1 Hanus, C. & Schuman, E. M. Proteostasis in complex dendrites. *Nat. Rev. Neurosci.* **14**, 638–648 (2013).
- 2 Malenka, R. C. & Bear, M. F. LTP and LTD: an embarrassment of riches. *Neuron* **44**, 5–21 (2004).
- 3 Nicoll, R. A. A Brief History of Long-Term Potentiation. *Neuron* **93**, 281–290 (2017).
- 4 Anggono, V. & Huganir, R. L. Regulation of AMPA receptor trafficking and synaptic plasticity. *Curr. Opin. Neurobiol.* **22**, 461–469 (2012).
- 5 Grant, S. G. N. Synaptopathies: diseases of the synaptome. *Curr. Opin. Neurobiol.* **22**, 522–529 (2012).
- 6 de Wit, J. & Ghosh, A. Specification of synaptic connectivity by cell surface interactions. *Nat. Rev. Neurosci.* **17**, 22–35 (2016).
- 7 Südhof, T. C. Towards an Understanding of Synapse Formation. *Neuron* **100**, 276–293 (2018).
- 8 Antebi, Y. E. *et al.* Combinatorial Signal Perception in the BMP Pathway. *Cell* **170**, 1184–1196.e24 (2017).
- 9 Sharma, K. *et al.* Cell type- and brain region-resolved mouse brain proteome. *Nat. Neurosci.* **18**, 1819–1831 (2015).
- 10 Alvarez-Castelao, B. *et al.* Cell-type-specific metabolic labeling of nascent proteomes in vivo. *Nat. Biotechnol.* **35**, 1196–1201 (2017).
- 11 Frese, C. K. *et al.* Quantitative Map of Proteome Dynamics during Neuronal Differentiation. *Cell Rep.* **18**, 1527–1542 (2017).
- 12 Schanzenbächer, C. T., Sambandan, S., Langer, J. D. & Schuman, E. M. Nascent Proteome Remodeling following Homeostatic Scaling at Hippocampal Synapses. *Neuron* **92**, 358–371 (2016).
- 13 Schanzenbächer, C. T., Langer, J. D. & Schuman, E. M. Time- and polarity-dependent proteomic changes associated with homeostatic scaling at central synapses. *Elife* **7**, (2018).
- 14 Takamori, S. *et al.* Molecular anatomy of a trafficking organelle. *Cell* **127**, 831–846 (2006).
- 15 Bayés, A. *et al.* Characterization of the proteome, diseases and evolution of the human postsynaptic density. *Nat. Neurosci.* **14**, 19–21 (2011).
- 16 Uezu, A. *et al.* Identification of an elaborate complex mediating postsynaptic inhibition. *Science* **353**, 1123–1129 (2016).
- 17 Roy, M. *et al.* Proteomic analysis of postsynaptic proteins in regions of the human neocortex. *Nat. Neurosci.* **21**, 130–138 (2018).
- 18 Boyken, J. *et al.* Molecular profiling of synaptic vesicle docking sites reveals novel proteins but few differences between glutamatergic and GABAergic synapses. *Neuron* **78**, 285–297 (2013).
- 19 Biesemann, C. *et al.* Proteomic screening of glutamatergic mouse brain synaptosomes isolated by fluorescence activated sorting. *EMBO J.* **33**, 157–170 (2014).
- 20 Loh, K. H. *et al.* Proteomic Analysis of Unbounded Cellular Compartments: Synaptic Clefts. *Cell* **166**, 1295–1307.e21 (2016).
- 21 Cagnetta, R., Frese, C. K., Shigeoka, T., Krijgsveld, J. & Holt, C. E. Rapid Cue-Specific Remodeling of the Nascent Axonal Proteome. *Neuron* doi:10.1016/j.neuron.2018.06.004
- 22 Schwenk, J. *et al.* Regional Diversity and Developmental Dynamics of the AMPA-Receptor Proteome in the Mammalian Brain. *Neuron* **84**, 41–54 (2014).
- 23 Schwenk, J. *et al.* High-resolution proteomics unravel architecture and molecular diversity of native AMPA receptor complexes. *Neuron* **74**, 621–633 (2012).
- 24 Schwenk, J. *et al.* Native GABAB receptors are heteromultimers with a family of

- auxiliary subunits. *Nature* **465**, 231–235 (2010).
25. Schwenk, J. *et al.* Modular composition and dynamics of native GABAB receptors identified by high-resolution proteomics. *Nat. Neurosci.* **19**, 233–242 (2016).
 26. Itzhak, D. N. *et al.* A Mass Spectrometry-Based Approach for Mapping Protein Subcellular Localization Reveals the Spatial Proteome of Mouse Primary Neurons. *Cell Rep.* **20**, 2706–2718 (2017).
 27. Herber, J. *et al.* Click Chemistry-mediated Biotinylation Reveals a Function for the Protease BACE1 in Modulating the Neuronal Surface Glycoproteome. *Mol. Cell. Proteomics* **17**, 1487–1501 (2018).
 28. Kuhn, P.-H. *et al.* Systematic substrate identification indicates a central role for the metalloprotease ADAM10 in axon targeting and synapse function. *Elife* **5**, (2016).
 29. Lundberg, E. & Borner, G. H. H. Spatial proteomics: a powerful discovery tool for cell biology. *Nat. Rev. Mol. Cell Biol.* (2019). doi:10.1038/s41580-018-0094-y
 30. van Oostrum, M. *et al.* De novo Classification of Mouse B Cell Types using Surfaceome Proteotype Maps. doi:10.1101/620344
 31. Wollscheid, B. *et al.* Mass-spectrometric identification and relative quantification of N-linked cell surface glycoproteins. *Nat. Biotechnol.* **27**, 378–386 (2009).
 32. Gillet, L. C. *et al.* Targeted data extraction of the MS/MS spectra generated by data-independent acquisition: a new concept for consistent and accurate proteome analysis. *Mol. Cell. Proteomics* **11**, O111.016717 (2012).
 33. Boheler, K. R. *et al.* A human pluripotent stem cell surface N-glycoproteome resource reveals markers, extracellular epitopes, and drug targets. *Stem cell reports* **3**, 185–203 (2014).
 34. Hofmann, A., Bausch-Fluck, D. & Wollscheid, B. CSC technology: selective labeling of glycoproteins by mild oxidation to phenotype cells. *Methods Mol. Biol.* **951**, 33–43 (2013).
 35. Bausch-Fluck, D. *et al.* A mass spectrometric-derived cell surface protein atlas. *PLoS One* **10**, e0121314 (2015).
 36. Dotti, C. G., Sullivan, C. A. & Banker, G. A. The establishment of polarity by hippocampal neurons in culture. *J. Neurosci.* **8**, 1454–1468 (1988).
 37. van Spronsen, M. *et al.* Developmental and activity-dependent miRNA expression profiling in primary hippocampal neuron cultures. *PLoS One* **8**, e74907 (2013).
 38. Bruderer, R. *et al.* Extending the limits of quantitative proteome profiling with data-independent acquisition and application to acetaminophen-treated three-dimensional liver microtissues. *Mol. Cell. Proteomics* **14**, 1400–1410 (2015).
 39. Bruderer, R. *et al.* Optimization of Experimental Parameters in Data-Independent Mass Spectrometry Significantly Increases Depth and Reproducibility of Results. *Mol. Cell. Proteomics* (2017). doi:10.1074/mcp.RA117.000314
 40. Kumar, L. & E Futschik, M. Mfuzz: a software package for soft clustering of microarray data. *Bioinformatics* **2**, 5–7 (2007).
 41. Schwämmle, V. & Jensen, O. N. A simple and fast method to determine the parameters for fuzzy c-means cluster analysis. *Bioinformatics* **26**, 2841–2848 (2010).
 42. Mabb, A. M. & Ehlers, M. D. Ubiquitination in postsynaptic function and plasticity. *Annu. Rev. Cell Dev. Biol.* **26**, 179–210 (2010).
 43. Goo, M. S. *et al.* Activity-dependent trafficking of lysosomes in dendrites and dendritic spines. *J. Cell Biol.* **216**, 2499–2513 (2017).
 44. Hanus, C. & Ehlers, M. D. Specialization of biosynthetic membrane trafficking for neuronal form and function. *Curr. Opin. Neurobiol.* **39**, 8–16 (2016).
 45. Giurgiu, M. *et al.* CORUM: the comprehensive resource of mammalian protein complexes-2019. *Nucleic Acids Res.* **47**, D559–D563 (2019).
 46. Földy, C. *et al.* Single-cell RNAseq reveals cell adhesion molecule profiles in

- electrophysiologically defined neurons. *Proc. Natl. Acad. Sci. U. S. A.* **113**, E5222–31 (2016).
47. Fritschy, J.-M., Panzanelli, P. & Tyagarajan, S. K. Molecular and functional heterogeneity of GABAergic synapses. *Cell. Mol. Life Sci.* **69**, 2485–2499 (2012).
 48. Zhang, Y. *et al.* An RNA-sequencing transcriptome and splicing database of glia, neurons, and vascular cells of the cerebral cortex. *J. Neurosci.* **34**, 11929–11947 (2014).
 49. Chechik, G. & Koller, D. Timing of gene expression responses to environmental changes. *J. Comput. Biol.* **16**, 279–290 (2009).
 50. Sander, J., Schultze, J. L. & Yosef, N. ImpulseDE: detection of differentially expressed genes in time series data using impulse models. *Bioinformatics* **33**, 757–759 (2017).
 51. Lee, S.-J. *et al.* Presynaptic Neuronal Pentraxin Receptor Organizes Excitatory and Inhibitory Synapses. *J. Neurosci.* **37**, 1062–1080 (2017).
 52. Diering, G. H. & Hugarir, R. L. The AMPA Receptor Code of Synaptic Plasticity. *Neuron* **100**, 314–329 (2018).
 53. Turrigiano, G. G. The self-tuning neuron: synaptic scaling of excitatory synapses. *Cell* **135**, 422–435 (2008).
 54. Wierenga, C. J., Iyata, K. & Turrigiano, G. G. Postsynaptic expression of homeostatic plasticity at neocortical synapses. *J. Neurosci.* **25**, 2895–2905 (2005).
 55. Iyata, K., Sun, Q. & Turrigiano, G. G. Rapid synaptic scaling induced by changes in postsynaptic firing. *Neuron* **57**, 819–826 (2008).
 56. Schaukowitz, K. *et al.* An Intrinsic Transcriptional Program Underlying Synaptic Scaling during Activity Suppression. *Cell Rep.* **18**, 1512–1526 (2017).
 57. Peng, Y.-R., Hou, Z.-H. & Yu, X. The kinase activity of EphA4 mediates homeostatic scaling-down of synaptic strength via activation of Cdk5. *Neuropharmacology* **65**, 232–243 (2013).
 58. Nguyen, T. A. *et al.* SIDT2 Transports Extracellular dsRNA into the Cytoplasm for Innate Immune Recognition. *Immunity* **47**, 498–509.e6 (2017).
 59. Takahashi, M. *et al.* SIDT2 mediates gymnosis, the uptake of naked single-stranded oligonucleotides into living cells. *RNA Biol.* **14**, 1534–1543 (2017).
 60. Jurado, S. *et al.* LTP requires a unique postsynaptic SNARE fusion machinery. *Neuron* **77**, 542–558 (2013).
 61. Opazo, P. & Choquet, D. A three-step model for the synaptic recruitment of AMPA receptors. *Mol. Cell. Neurosci.* **46**, 1–8 (2011).
 62. Penn, A. C. *et al.* Hippocampal LTP and contextual learning require surface diffusion of AMPA receptors. *Nature* **549**, 384–388 (2017).
 63. Makino, H. & Malinow, R. AMPA receptor incorporation into synapses during LTP: the role of lateral movement and exocytosis. *Neuron* **64**, 381–390 (2009).
 64. Granger, A. J., Shi, Y., Lu, W., Cerpas, M. & Nicoll, R. A. LTP requires a reserve pool of glutamate receptors independent of subunit type. *Nature* **493**, 495–500 (2013).
 65. Choquet, D. Linking Nanoscale Dynamics of AMPA Receptor Organization to Plasticity of Excitatory Synapses and Learning. *J. Neurosci.* **38**, 9318–9329 (2018).
 66. Harward, S. C., Hedrick, N. G., Hall, C. E. & Parra-Bueno, P. Autocrine BDNF–TrkB signalling within a single dendritic spine. *Nature* (2016).
 67. Hafner, A.-S. *et al.* Lengthening of the Stargazin Cytoplasmic Tail Increases Synaptic Transmission by Promoting Interaction to Deeper Domains of PSD-95. *Neuron* **86**, 475–489 (2015).
 68. Curtis, J., Errington, M., Bliss, T., Voss, K. & MacLeod, N. Age-dependent loss of PTP and LTP in the hippocampus of PrP-null mice. *Neurobiol. Dis.* **13**, 55–62 (2003).
 69. Chen, C.-M. *et al.* Wnt5a is essential for hippocampal dendritic maintenance and spatial learning and memory in adult mice. *Proc. Natl. Acad. Sci. U. S. A.* (2017).

doi:10.1073/pnas.1615792114

70. Chen, X. *et al.* Ablation of Type III Adenylyl Cyclase in Mice Causes Reduced Neuronal Activity, Altered Sleep Pattern, and Depression-like Phenotypes. *Biol. Psychiatry* **80**, 836–848 (2016).
71. Jing, J. *et al.* Proteomic mapping of ER-PM junctions identifies STIMATE as a regulator of Ca²⁺ influx. *Nat. Cell Biol.* **17**, 1339–1347 (2015).
72. Syeda, R. *et al.* LRRC8 Proteins Form Volume-Regulated Anion Channels that Sense Ionic Strength. *Cell* **164**, 499–511 (2016).
73. Voss, F. K. *et al.* Identification of LRRC8 heteromers as an essential component of the volume-regulated anion channel VRAC. *Science* **344**, 634–638 (2014).
74. Südhof, T. C. Synaptic Neurexin Complexes: A Molecular Code for the Logic of Neural Circuits. *Cell* **171**, 745–769 (2017).
75. Nandagopal, N. *et al.* Dynamic Ligand Discrimination in the Notch Signaling Pathway. *Cell* (2018). doi:10.1016/j.cell.2018.01.002
76. Mahdavi, A. *et al.* Engineered Aminoacyl-tRNA Synthetase for Cell-Selective Analysis of Mammalian Protein Synthesis. *J. Am. Chem. Soc.* **138**, 4278–4281 (2016).
77. Moremen, K. W., Tiemeyer, M. & Nairn, A. V. Vertebrate protein glycosylation: diversity, synthesis and function. *Nat. Rev. Mol. Cell Biol.* **13**, 448–462 (2012).
78. Bausch-Fluck, D. *et al.* The in silico human surfaceome. *Proceedings of the National Academy of Sciences* 201808790 (2018).
79. Schwenk, J. *et al.* Functional proteomics identify cornichon proteins as auxiliary subunits of AMPA receptors. *Science* **323**, 1313–1319 (2009).
80. Telley, L. *et al.* Sequential transcriptional waves direct the differentiation of newborn neurons in the mouse neocortex. *Science* **351**, 1443–1446 (2016).
81. Sigler, A. *et al.* Formation and Maintenance of Functional Spines in the Absence of Presynaptic Glutamate Release. *Neuron* **94**, 304–311.e4 (2017).
82. Kwon, H.-B. & Sabatini, B. L. Glutamate induces de novo growth of functional spines in developing cortex. *Nature* **474**, 100–104 (2011).
83. Oh, W. C., Lutz, S., Castillo, P. E. & Kwon, H.-B. De novo synaptogenesis induced by GABA in the developing mouse cortex. *Science* **353**, 1037–1040 (2016).
84. Diering, G. H., Gustina, A. S. & Huganir, R. L. PKA-GluA1 Coupling via AKAP5 Controls AMPA Receptor Phosphorylation and Cell-Surface Targeting during Bidirectional Homeostatic Plasticity. *Neuron* **84**, 790–805 (2014).
85. Dzyubenko, E., Rozenberg, A., Hermann, D. M. & Faissner, A. Colocalization of synapse marker proteins evaluated by STED-microscopy reveals patterns of neuronal synapse distribution in vitro. *J. Neurosci. Methods* **273**, 149–159 (2016).
86. Stamou, M., Grodzki, A. C., van Oostrum, M., Wollscheid, B. & Lein, P. J. Fc gamma receptors are expressed in the developing rat brain and activate downstream signaling molecules upon cross-linking with immune complex. *J. Neuroinflammation* **15**, 7 (2018).
87. Tyagarajan, S. K. & Ghosh, H. Regulation of GABAergic synapse formation and plasticity by GSK3β-dependent phosphorylation of gephyrin. *Proceedings of the* (2011).
88. Larsen, D., Pittelkow, M., Karmakar, S. & Kool, E. T. New organocatalyst scaffolds with high activity in promoting hydrazone and oxime formation at neutral pH. *Org. Lett.* **17**, 274–277 (2015).
89. Perez-Riverol, Y. *et al.* The PRIDE database and related tools and resources in 2019: improving support for quantification data. *Nucleic Acids Res.* **47**, D442–D450 (2019).
90. Blattmann, P. *et al.* Generation of a zebrafish SWATH-MS spectral library to quantify 10,000 proteins. *Sci Data* **6**, 190011 (2019).
91. Choi, M. *et al.* MSstats: an R package for statistical analysis of quantitative mass spectrometry-based proteomic experiments. *Bioinformatics* **30**, 2524–2526 (2014).

92. Conway, J. R., Lex, A. & Gehlenborg, N. UpSetR: an R package for the visualization of intersecting sets and their properties. *Bioinformatics* (2017).
93. Kuleshov, M. V. *et al.* Enrichr: a comprehensive gene set enrichment analysis web server 2016 update. *Nucleic Acids Res.* **44**, W90–7 (2016).
94. Alexa, A. & Rahnenfuhrer, J. topGO: enrichment analysis for gene ontology. *R package version 2*, 2010 (2010).